HAL open science

Microtubules self-repair in living cells

Morgan Gazzola, Alexandre Schaeffer, Ciarán Butler-Hallissey, Karoline Friedl, Benoit Vianay, Jérémie Gaillard, Christophe Leterrier, Laurent Blanchoin, Manuel Théry

To cite this version:

Morgan Gazzola, Alexandre Schaeffer, Ciarán Butler-Hallissey, Karoline Friedl, Benoit Vianay, et al.. Microtubules self-repair in living cells. Current Biology - CB, 2023, 33 (1), pp.122 - 133.e4. 10.1016/j.cub.2022.11.060 . hal-04220738v2

HAL Id: hal-04220738

https://hal.science/hal-04220738v2

Submitted on 4 Oct 2023

HAL is a multi-disciplinary open access archive for the deposit and dissemination of scientific research documents, whether they are published or not. The documents may come from teaching and research institutions in France or abroad, or from public or private research centers.

L'archive ouverte pluridisciplinaire **HAL**, est destinée au dépôt et à la diffusion de documents scientifiques de niveau recherche, publiés ou non, émanant des établissements d'enseignement et de recherche français ou étrangers, des laboratoires publics ou privés.

Article

Current Biology

Microtubules self-repair in living cells

Graphical abstract

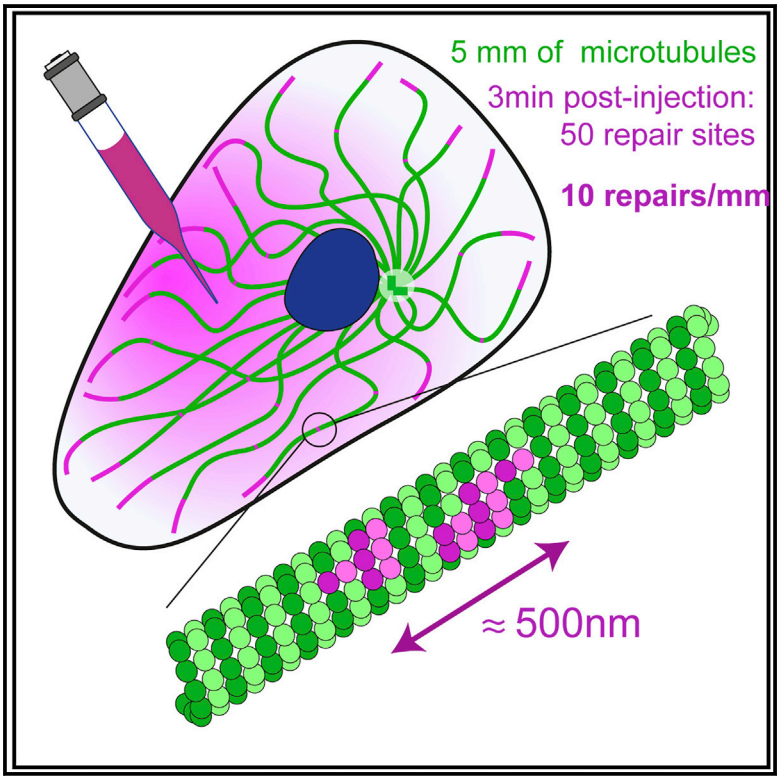

Highlights

- Free tubulin dimers can incorporate within the shaft of microtubules in living cells
- Most incorporations were smaller than 700 nm
- On average, incorporations can be detected every 100 μm of microtubule
- They are more frequent where the lateral fluctuations of microtubules are greater

Authors

Morgan Gazzola, Alexandre Schaeffer, Ciarán Butler-Hallissey, ..., Christophe Leterrier, Laurent Blanchoin, Manuel Théry

Correspondence

laurent.blanchoin@cea.fr (L.B.), manuel.thery@cea.fr (M.T.)

In brief

Using microinjection of fluorescent tubulin dimers, Gazzola et al. show that free dimers can incorporate in the lattice of pre-existing microtubules in living cells. A few minutes after injection, incorporations can be detected throughout the network of microtubules. This demonstrates that microtubules constantly self-repair in living cells.

Gazzola et al., 2023, Current Biology *33*, 1–12
January 9, 2023 © 2022 Elsevier Inc.
https://doi.org/10.1016/j.cub.2022.11.060

CellPress

Please cite this article in press as: Gazzola et al., Microtubules self-repair in living cells, Current Biology (2022), https://doi.org/10.1016/j.cub.2022.11.060

Current Biology

CellPress

Article

Microtubules self-repair in living cells

Morgan Gazzola,[1] Alexandre Schaeffer,[1] Ciarán Butler-Hallissey,[2] Karoline Friedl,[2,3] Benoit Vianay,[1] Jérémie Gaillard,[4] Christophe Leterrier,[2] Laurent Blanchoin,[4,5,*] and Manuel Théry[1,6,7,*]
[1]University of Paris, INSERM, CEA, UMRS1160, Institut de Recherche Saint Louis, CytoMorpho Lab, Hôpital Saint Louis, 10 Avenue Claude Vellefaux, 75010 Paris, France
[2]Aix Marseille Université, CNRS, INP UMR7051, NeuroCyto Lab, 27 Boulevard Jean Moulin, 13385 Marseille, France
[3]Abbelight, 191 Avenue Aristide Briand, 94230 Cachan, France
[4]University of Grenoble-Alpes, CEA, CNRS, UMR5168, Interdisciplinary Research Institute of Grenoble, CytoMorpho Lab, 17 rue des Martyrs, 38054 Grenoble, France
[5]Twitter: @LBlanchoin
[6]Twitter: @ManuelThery
[7]Lead contact
*Correspondence: laurent.blanchoin@cea.fr (L. B.), manuel.thery@cea.fr (M. T.)
https://doi.org/10.1016/j.cub.2022.11.060

SUMMARY

Microtubule self-repair has been studied both *in vitro* and *in vivo* as an underlying mechanism of microtubule stability. The turnover of tubulin dimers along the microtubule has challenged the pre-existing dogma that only growing ends are dynamic. However, although there is clear evidence of tubulin incorporation into the shaft of polymerized microtubules *in vitro*, the possibility of such events occurring in living cells remains uncertain. In this study, we investigated this possibility by microinjecting purified tubulin dimers labeled with a red fluorophore into the cytoplasm of cells expressing GFP-tubulin. We observed the appearance of red dots along the pre-existing green microtubule within minutes. We found that the fluorescence intensities of these red dots were inversely correlated with the green signal, suggesting that the red dimers were incorporated into the microtubules and replaced the pre-existing green dimers. Lateral distance from the microtubule center was similar to that in incorporation sites and in growing ends. The saturation of the size and spatial frequency of incorporations as a function of injected tubulin concentration and post-injection delay suggested that the injected dimers incorporated into a finite number of damaged sites. By our low estimate, within a few minutes of the injections, free dimers incorporated into major repair sites every 70 μm of microtubules. Finally, we mapped the location of these sites in micropatterned cells and found that they were more concentrated in regions where the actin filament network was less dense and where microtubules exhibited greater lateral fluctuations.

INTRODUCTION

Microtubules are polar and dynamic polymers running through the cytoplasm of eukaryotic cells. They serve as tracks for molecular motors and, as such, play essential roles in key cellular processes such as cell polarity, migration, division, and more generally to the global regulation of intracellular organization.[1] They result from the self-assembly of tubulin dimers into twelve to fourteen protofilaments that align longitudinally to form a hollow tube. Tubulin dimers are thus densely packed and highly organized into a pseudocrystalline structure named the microtubule lattice.[2,3] Microtubules dynamics is characterized by the alternance between growing and shrinking phases resulting from the addition and removal of tubulin dimers at the end of microtubules.[4–6] However, in the last decade, it has been proposed that tubulin dimers could also be exchanged along the microtubule shaft in a self-renewal process of the lattice.[7,8]

Microtubules that were polymerized *in vitro* and further capped to prevent ends shortening were found to form kinks following the removal of free surrounding tubulin.[9] Interestingly, these microtubules were capable to recover their linear shape after the re-addition of free dimers.[9] This was suggestive of the loss and reincorporation of tubulin dimers in the lattice of microtubules, a hypothesis further demonstrated by the visualization of this process with fluorescent tubulin dimers.[10] These exchanges were suggested to occur at specific defect sites where the lattice structure displayed defects such as missing dimers or dislocation in the organization of protofilaments.[10–13] This hypothesis is consistent with the analysis of microtubule response to bending cycles during which they appeared to soften in a non-elastic response and were further seen to recover their initial mechanical state by the incorporation of new dimers in their damaged lattice.[14]

Tubulin dimers were even seen to incorporate into large sections in the shaft of Taxol-stabilized microtubules.[15] Such large incorporations of free dimers in damaged lattice have also been observed in response to the activity of severing enzymes,[16,17] oxidative stress,[18] and even the walk of molecular motors.[19] Synergistically, specific microtubule-associated proteins could either promote the incorporations of tubulin dimers

Please cite this article in press as: Gazzola et al., Microtubules self-repair in living cells, Current Biology (2022), https://doi.org/10.1016/j.cub.2022.11.060

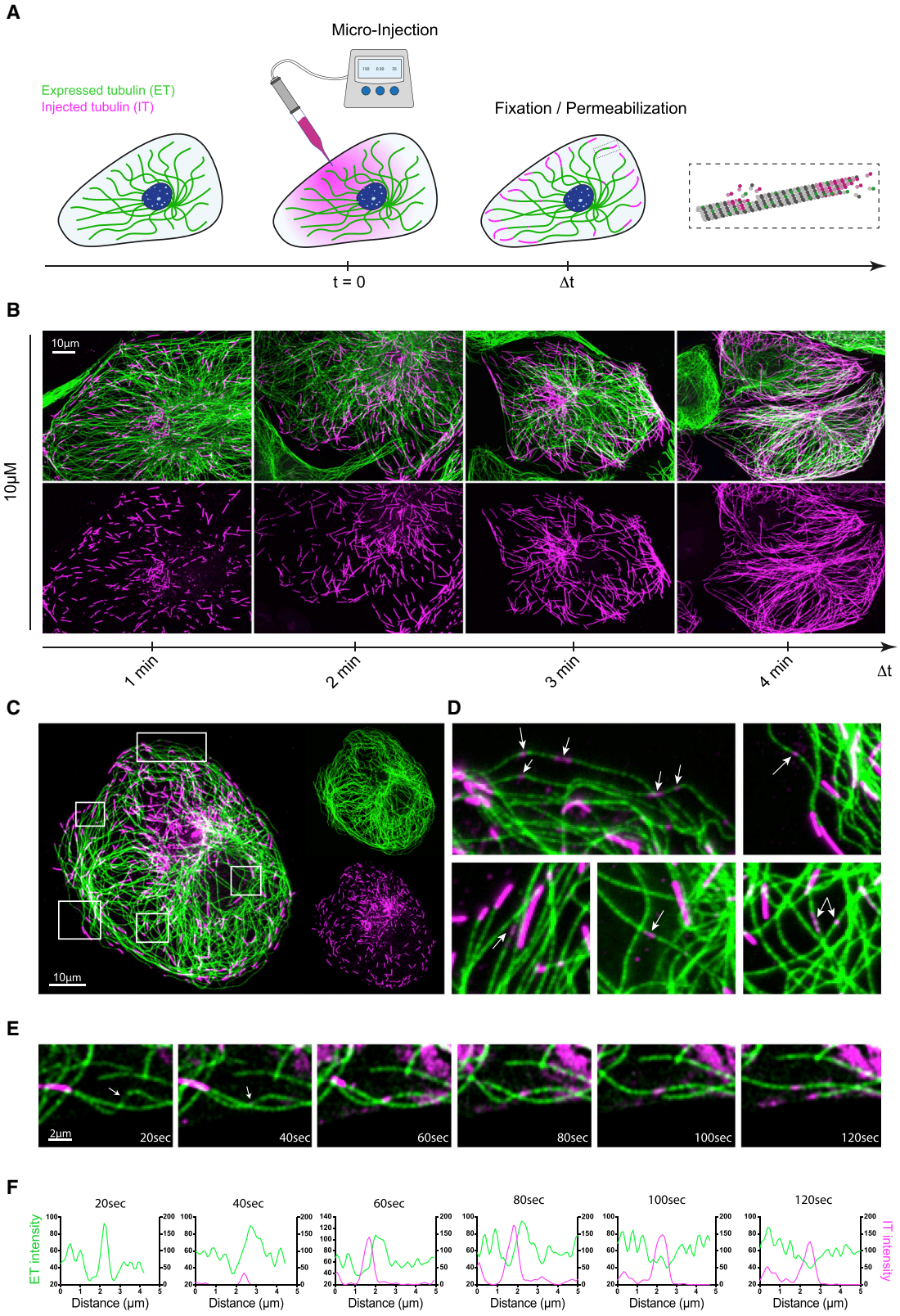

(legend on next page)

Please cite this article in press as: Gazzola et al., Microtubules self-repair in living cells, Current Biology (2022), https://doi.org/10.1016/j.cub.2022.11.060

CellPress

or act as a scaffold to protect damaged microtubule lattice.[17,20] Overall, the latest *in vitro* studies challenged the rules of microtubule dynamics being restricted to the end and redefined the lattice as a dynamic and self-repairing structure.

Unfortunately, in living cells, the investigation of microtubule self-repair has been more challenging. Experiments with photoconvertible tubulin were limited by the weakness of the signal, and the formation of aggregates that could incorporate during microtubules polymerization.[21] Moreover, although structural defect or larger damaged regions were undoubtedly observed in the microtubule lattice of mammalian cells by cryoelectron microscopy,[22–24] the incorporation of tubulin dimers in these regions has never been documented. Physical injuries or molecular motors overexpression were recently shown to increase microtubule length and network density in migratory cells and thus were suggestive of a self-repair mechanism.[21,25] In addition, the entry of small peptides in the microtubule's lumen implied the presence of sufficiently large opening in the microtubule lattice.[26] Finally, markers of tubulin dimers in a GTP-like conformation, i.e., newly added tubulin or locally damaged lattices, such as hMB11 or CLIP-170, were observed along the length of microtubules in living cells.[27,28] Although these results were suggestive of microtubule self-repair in living cells, they did not constitute clear evidence of its actual occurrence nor did they provide any quantitative description of its manifestation.

Here, to investigate the potential incorporation of tubulin dimers in pre-existing microtubules, we microinjected fluorescently labeled tubulin dimers in the cytoplasm of living cells. Our data demonstrate that injected dimers were not only recruited to microtubule growing ends but also within the microtubule lattice in a specific manner.

RESULTS

Free tubulin dimers can form patches along pre-existing microtubules

Microinjection of biotin-bound tubulin dimers was used in early studies to investigate the localization of microtubules polymerizing sites.[29,30] Immuno-labeling of endogenous and injected dimers clearly revealed the addition of dimers at the end of microtubules, but this technique may not provide the required specificity to undoubtedly characterize repair sites. To circumvent the use of immunolabeling, we microinjected purified tubulin labeled with ATTO-565, which we further referred to as injected tubulin (IT) (displayed in figures in magenta), in the cytoplasm of PtK2 cells expressing GFP-tubulin, which we further referred to as expressed tubulin (ET) (displayed in figures in green) (Figure 1A). As expected from previous studies,[29] about half of the microtubule network got renewed in the 4 min following microinjection of 10 μM tubulin dimers (Figure 1B). The visualization and evaluation of potential repair sites appeared challenging in such a densely labeled network. We thus analyzed the tubulin content of pre-existing microtubules only 2 min after the microinjection (Figure 1C). Interestingly, we could observe the presence of patches of red-fluorescent IT in several microtubules despite the short delay after the injection (Figure 1D, white arrows, more examples shown in Figure S1A). We could also monitor the behavior of red-fluorescent IT and green-fluorescent MTs in live, at the very edge of flat cells, where the cytoplasmic background is low and found that IT patches could form in less than a minute along pre-existing MTs (Figures 1E and 1F; Video S1).

However, the presence of those patches distant from growing ends was insufficient to ascertain their origin. Indeed, they could result from IT incorporation within the lattice, IT binding along the side of microtubule shaft or even the annealing between two microtubules growing ends.

Intensity of newly injected dimers in patches anti-correlates with the intensity of pre-existing dimers in the lattice

Following microinjection, growing microtubules were composed of unlabeled endogenous tubulin dimers (endogenous tubulin), genetically expressed green-fluorescent dimers (ET) and microinjected red-fluorescent dimers (IT) (Figure 2A). We reasoned that if the IT dimers replaced the endogenous and the ET dimers, an anticorrelation between the green and the red fluorescence could be observed. However, if IT dimers were bound to the side of the microtubule lattice, the two intensities should not be related. We thus measured intensity profiles along microtubules displaying red patches along their length. We found that the presence of IT patches along microtubules was associated to a decrease in ET intensities (Figure 2B; more examples shown in Figure S2A), supporting the hypothesis of a genuine incorporation in the lattice rather than a side-binding of the dimers. Moreover, IT intensities measured in IT patches were always lower than the IT intensities measured at microtubule's growing ends (Figures 2B, S2B, and S2C). This result ruled out the

Figure 1. Injected tubulins form patches along the length of the microtubules and polymerize at their growing ends

(A) Schematic representation of the microinjection protocol. Purified ATTO-565-labeled tubulin (magenta) is microinjected in PtK2 cells expressing GFP-tubulin (green). Following the microinjection, injected ATTO-565-tubulin (IT) freely diffuses throughout the cell's cytoplasm. Cells are then pre-permeabilized, fixed, and imaged. Right: enlarged region illustrating how IT can form patches along the microtubule's shaft and assemble at the growing end.

(B) Self-renewal of the microtubule network in PtK2 GFP-tubulin cells injected with 10 μM IT. Z acquisitions were performed and projected on a single image containing the maximal intensity of each pixel. Images show the newly assembled parts of the microtubule network 1, 2, 3, and 4 min post-injection. Scale bars, 10 μm.

(C) A PTK2 GFP-tubulin cell (ET signal is shown in green) microinjected with 10 μM IT (IT signal is shown in magenta). Z acquisitions were performed and projected on a single image containing the maximal intensity of each pixel. Scale bars, 10 μm.

(D) Images correspond to white insets shown in (C). Arrows point at IT patches (small magenta spots) that are localized along pre-existing microtubules (green) at a distance from microtubules growing ends (long magenta stretches).

(E) Images corresponding to the live acquisition of an IT patch appearance on a microtubule in the very edge of a flat cell. The acquisition was made 2–3 min after the injection of 10 μM IT every 20 s for 180 s on a spinning disk confocal microscope.

(F) Fluorescence intensity profiles of the microtubule showing the IT patch over time.

See also Figure S1 and Video S1.

Please cite this article in press as: Gazzola et al., Microtubules self-repair in living cells, Current Biology (2022), https://doi.org/10.1016/j.cub.2022.11.060

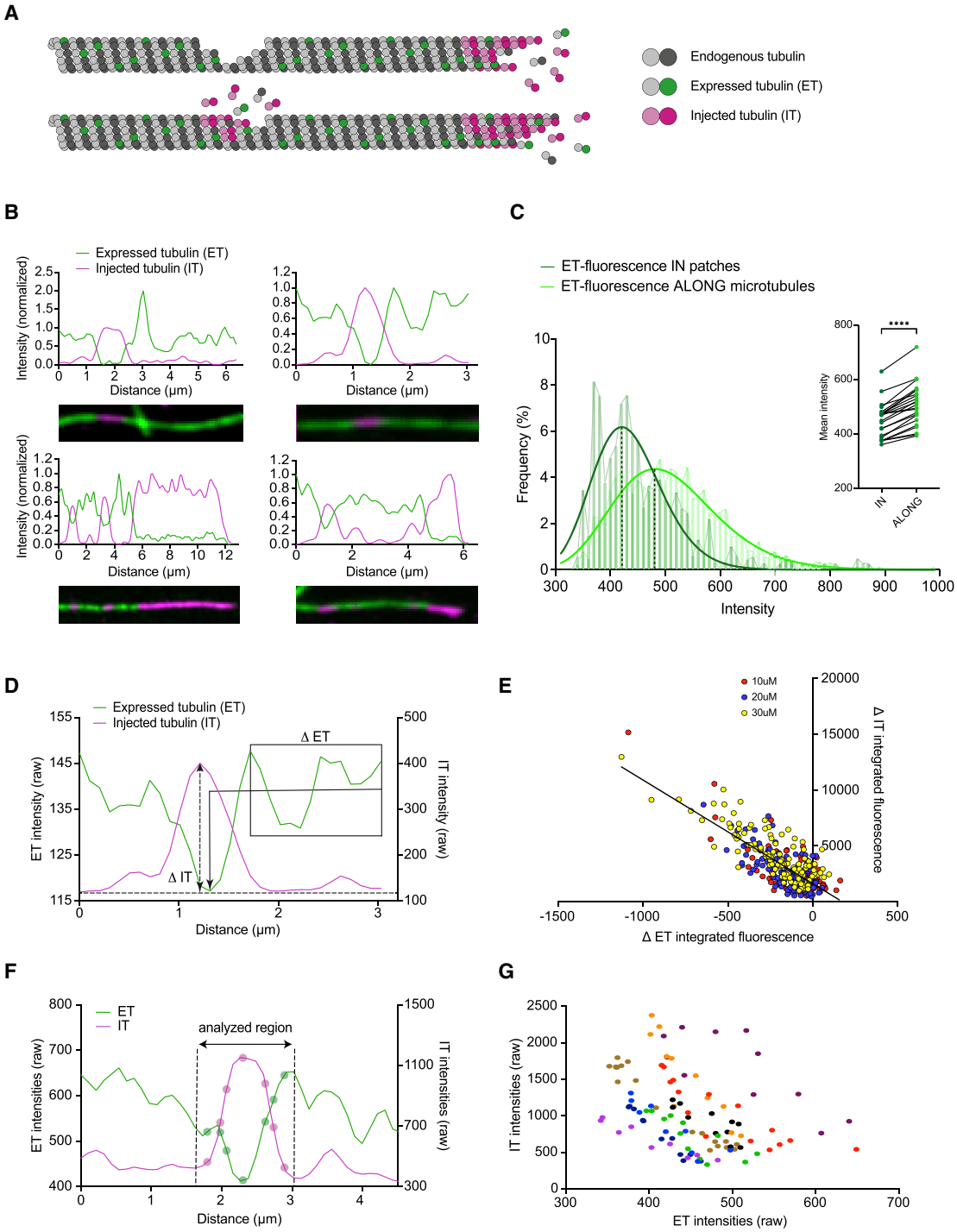

Figure 2. Anti-correlation between injected tubulin patches and fluorescence decrease of pre-existing lattice

(A) Schematic representation of the repair process of a damaged microtubule. Following injection of tubulin dimers, the growing end and the damaged region promote the co-assembly of unlabeled endogenous tubulin (gray), GFP-tagged expressed tubulin: ET (green), and ATTO-565-labeled injected tubulin: IT (magenta).

(B) Fluorescence intensity profiles of microtubules exhibiting a patch of IT. Profiles have been normalized to 1 for the shaft signal of ET and for the peak of IT.

(C) Histograms of ET-fluorescence intensity frequencies measured in IT patches or in adjacent sections of the microtubule with no detectable IT signal. Black-dotted lines indicate the means of the two ET fluorescence distributions. Inset represents the differences between the mean intensities of ET fluorescence measured in IT patches or in the adjacent section of the microtubule. n = 23 from thirteen individual cells. Statistical analysis was performed using two-tailed paired t test, ****$p < 0.0001$.

(legend continued on next page)

possibility of annealing between the growing ends of two pre-existing microtubules.

To further investigate the decrease in ET intensity in the IT patches, we compared ET intensities measured in IT patches to the ET intensity measured along the entire microtubules. ET intensities in IT patches were consistently lower than ET intensity along the rest of microtubules (Figure 2C). The average ET fluorescence measured along IT patches was 11.28% ± 4.84% lower than along microtubules (451.3 ± 64.93 versus 508.7 ± 77.30, mean ± SD) (Figure 2C), suggesting that the decrease resulted from a local and specific process rather than from random fluctuations that could be observed elsewhere along the lattice. In addition, the magnitude of the maximal ET decrease (ΔET) measured in the IT patch appeared anti-correlated with the maximal IT increase (ΔIT) (Figures 2D and 2E). Furthermore, point-by-point variations of intensities of the two signals within the patch were also clearly anti-correlated (Figures 2F, 2G, and S3A–S3C).

We also analyzed the precise localization of IT in the lattice with super-resolution STORM microscopy. We labeled purified tubulin dimers with Alexa Fluor 647 to visualize them in STORM and injected them at 10 μM into PtK2 cells. Two minutes later, cells were permeabilized, fixed, and immunostained with a CF680-tagged secondary antibody against α-tubulin to visualize both IT and the MTs with 2-color spectral STORM microscopy (Figure 3A). We confirmed the presence of patches of IT along MTs with this new labeling of tubulin dimers (Figure 3B). We then compared the localization of IT dimers in these patches (Figure 3C) and in microtubule growing ends (Figure 3D) where the polymerization process ensures that IT dimers were incorporated in the lattice. We averaged a hundred of cross-sectional line scans and found no difference in the width of the IT distribution in IT patches and in the microtubule growing ends, suggesting that in patches, IT dimers were not binding to the side of the lattice since this would have enlarged the width of their cross-sectional distribution (Figures 3C and 3D).

Taken together, our data strongly suggest that injected dimers replaced endogenous and expressed dimers in the lattice and that observed patches corresponded to genuine incorporations in pre-existing microtubules.

The incorporation process saturates with soluble tubulin concentration

To further investigate the biochemical regulation of new dimers addition in the pre-existing lattice of microtubules, we measured the variations of incorporations as a function of time and concentration. To investigate the temporal evolution of incorporations, we injected cells at a lower concentration, 5 μM, that allows the visualization of incorporations (Figure 4A) without interfering with the endogenous polymerization process. In fact, as previously described for other cytoskeletal filaments, the labeling of monomers directly interferes with their self-assembly[31] (Figures S3D and S3E). We measured the distribution length of the growing ends of the microtubules at various time points and evaluated their elongation rate at 4.2 μm/min, which is the typical range for the elongation of microtubule plus-ends [32] (Figures 4B, S3D, and S3E). The evolution of plus-ends length did not show any clear variation between the center and the edge of the cell, suggesting that the elongation process was rather homogeneous in the cell (Figure S4A).

We detected incorporations by segmenting and scanning the entire microtubule network using the SOAX software[33] (Figure 4C). Incorporations were segmented manually by selecting the patches whose IT intensities were at least twice higher than the background signal along microtubules (Figure S1B). The spatial frequency of incorporations per cell thus corresponded to the total number of incorporations divided by the length of the entire microtubule network. Strikingly, the length of incorporations did not evolve in the few minutes during which they could be clearly distinguished from microtubule ends (Figure 4D). However, their spatial frequency along MTs increased over time (Figure 4E). Noteworthy, the comparison of the total length of plus ends and incorporations suggested that the repair process represents less than 1% of the total assembly process.

To investigate the variation in size and frequency of plus ends and incorporations as a function of the IT concentration and to compare the two processes, we injected an increasing concentration of IT up to 40 μM and observed the network after 2–3 min. The intensity of IT in both plus ends (Figure 4F) and incorporations (Figure 4G) first increased and then saturated beyond 20 μM. It also corresponds to the maximum concentration of IT above which endogenous tubulin polymerization was blocked (Figures S3D and S3E). This showed that both processes were regulated by similar assembling rules. Similarly, the spatial frequency of incorporations followed the same trend and saturated above 20 μM (Figure 4H). Interestingly, the length of incorporations appeared independent of the IT concentration (Figure 4I). This trend was consistent with *in vitro* experiments[19] and supported the hypothesis that sites for incorporations have a limited length and that the incorporation did not propagate on the side of the pre-existing lattice. These observations contrast with the outcome of a non-specific adsorption along MTs, which would linearly increase in size and frequency with the concentration of IT.

Altogether, these results point at a saturation of the incorporation process, supporting the hypothesis of specific repair mechanism that is limited to a defined number of sites rather than a non-specific mechanism all along the length of microtubules.

(D) Illustration of the measurements of fluorescence intensity variations along the length of a microtubule displaying a patch of IT. The double arrowhead dotted line represents the difference measured between the highest IT-fluorescence intensity and the baseline (ΔIT). The black square with an arrowhead represents the difference measured between the mean ET-fluorescence intensity along the length of the microtubule and the lowest ET-fluorescence intensity in the patch (ΔET).
(E) Graph shows the values of ΔET and ΔIT measured as described in (D) in PtK2 GFP-tubulin cells microinjected with various concentrations of tubulin between 10 and 30 μM. n = 365 from twenty-nine individual cells.
(F) Illustration of the measurements of fluorescence intensities in a patch of IT. Circles correspond to measurement positions.
(G) Graph shows variations of ET and IT intensities in 9 different line scans measured in cells microinjected with 10, 20, or 30 μM tubulin (3 line scans per concentration). Distinct colors correspond to distinct microtubules.
See also Figures S2 and S3.

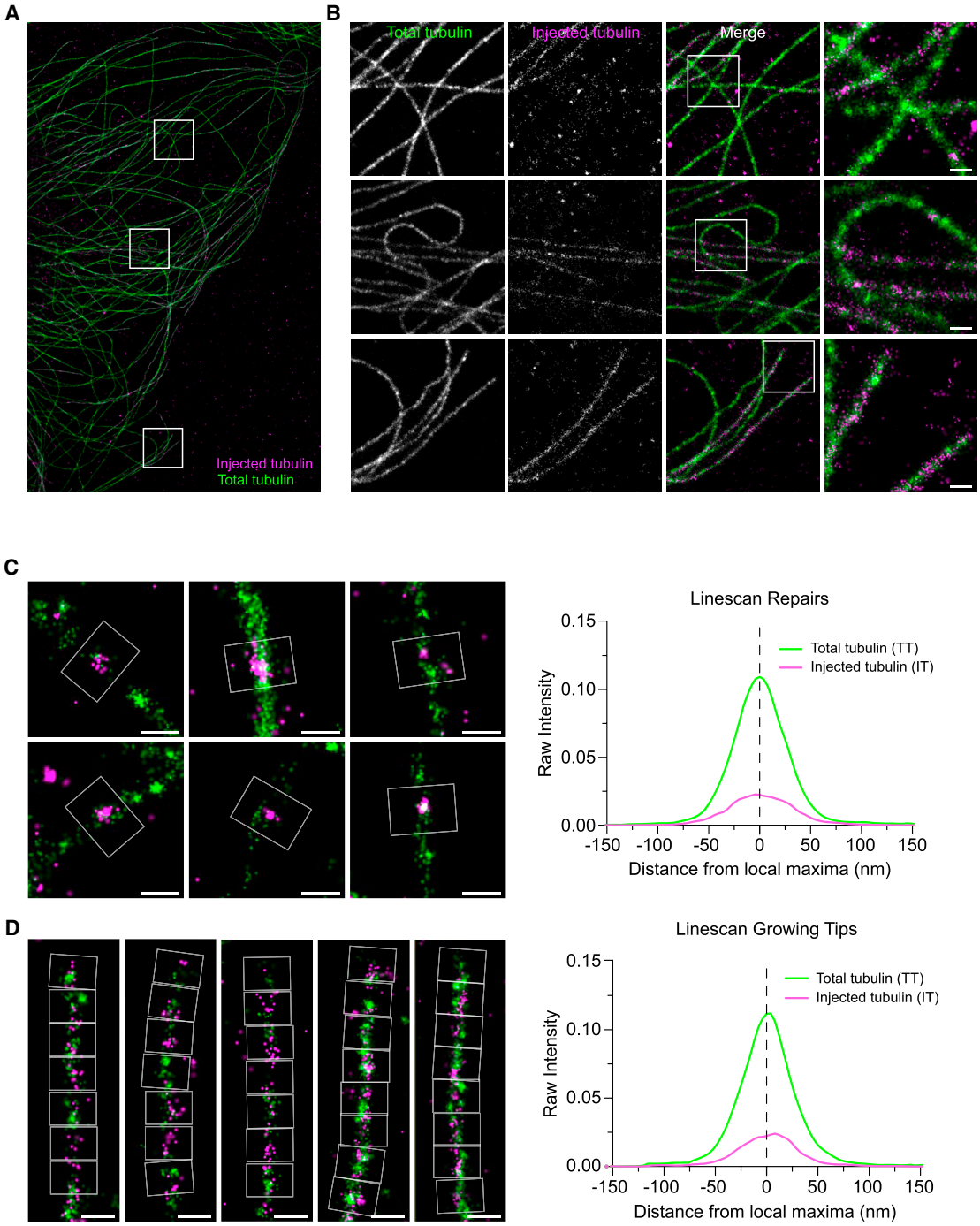

Figure 3. STORM microscopy provides nanoscale details of injected tubulin (IT) integration into the microtubule lattice and tip

(A) 10 μM AF647-tubulin (magenta, IT) was microinjected into the cytoplasm and allowed to freely diffuse 2–3 min before pre-permeabilization and fixation. Cells were immunostained with a CF680-tagged secondary antibody against α-tubulin to visualize total tubulin (green, TT) and imaged using 2-color spectral STORM. Single-molecule detection was performed with a low-intensity threshold (0.5) to provide an optimized labeling density and delineate continuous microtubules.

(B) Zoomed-in regions from (A) showing TT, IT, and a merge of these channels. The last column shows a higher zoom of the merged channels.

(C) Microtubules without IT polymerized tips were examined for repair sites. Here, the images were reconstructed from a standard intensity threshold detection of localization (1.0), for higher precision. Repair sites across 2 experiments from a total of 5 cells were analyzed using a 200-nm-thick line profile perpendicular to the microtubule (white boxes, n = 100 line ROIs analyzed). Intensity profiles across repairs were calculated for IT and TT, aligned to the position of intensity maximum for TT (estimated using a Gaussian fit), and then averaged and plotted.

(legend continued on next page)

We could thus evaluate the frequency of microtubule repair in saturating conditions (20 μM IT, 3 min post-injection) to be around 10 sites per mm of microtubules in PtK2 cells, i.e., a repair site every 100 μm in this 3 min-long time window.

Repair sites are not evenly distributed in the cell

Noteworthy, we observed that incorporations were longer in the vicinity of the injection site than in the cell periphery (Figures S4B and S4C). This showed that the injection flow can induce some damages along microtubules, as shown previously *in vitro*.[14,34] Fortunately, these experiments also showed that the injection flow did not propagate beyond 20–30 μm from the injection site (Video S2) and that repair sites could be observed in regions that were more distant than this critical length and thus not affected by this flow (Figures S4D and S4E). This showed that despite the damaging effect of the injection flow, the localization of repair sites and the variations of their subcellular density could be investigated in living cells. At first glance, it seemed that they were not evenly distributed all over the cell (Figure S4), suggesting that the repair process did not occur randomly on all microtubules.

To describe quantitatively the spatial distribution of incorporations in the microtubule network, we normalized cell shapes and internal architectures using micropatterns. Crossbow-shaped micropatterns direct the assembly of a lamella (transverse arcs and radial fibers) along the adhesive and curved edge (Figure 5A, upper part of the image) and stress fibers along non-adhesive and straight regions (Figure 5A, lower part of the image).[35] These actin structures are reproducible over many cells and do not fluctuate much in a period of 3 min (Figures 5B and 5C; Video S3). The microtubule network was denser at the cell center and along the adhesive and curved edges and less dense close to stress fibers (Figures 5D and 5E). Interestingly, although lateral fluctuations of microtubules could be observed throughout the cell cytoplasm, they were slightly more pronounced in the vicinity of stress fibers (Figure 5F; Video S4).

We microinjected red-fluorescent tubulin dimers in micropatterned cells to assess the localization of repair sites (Figure 5G). By reporting all the positions of incorporations detected over 34 cells (Figure S5A), we could generate a density map of their localization (Figure S5B). However, we noticed that high density of repair sites was located close to injection sites (Figure S5C). To alleviate this potential artifact, we ignored in all cells the repair sites that were detected in the vicinity of the injection site (Figure S5D). We overlaid these localization maps of repair sites (Figure 5H) and spatially averaged them to obtain a density map of incorporations sites (Figure 5I). Strikingly, this density map of incorporations did not correspond exactly to the density map of microtubules (Figure 5E), suggesting that locally the number of incorporations was not merely proportional to the length of microtubules. Indeed, incorporations were rarely observed along adhesive and curved edge where the network is dense. They were more frequent in regions adjacent to the stress fibers, where the actin network is more scarce. To quantitatively measure the local spatial frequencies of repair sites relatively to the local length of microtubule, we segmented microtubules and repair sites in individual cells (Figure 5J). We compared repair densities in regions facing distinct actin network architectures and found that they were more frequent toward the stress fibers (12.7 ± 6.2 per mm of microtubule) than toward the lamella (8.4 ± 4.5 per mm of microtubule) (Figure 5K). As a control, we compared the left and the right part of the cell, symmetric in terms of cell adhesion and actin architecture, and found no difference (10.8 ± 5.9 and 9.5 ± 4.5 incorporation per mm of microtubule) (Figure 5L). Interestingly, microtubule fluctuations were more intense in those regions with lower actin meshwork density,[36] suggesting that repair could be induced by local bending forces. Altogether, these results further confirmed the specificity of the repair process by revealing that it was not evenly distributed over the entire network. We concluded that incorporations were more frequent in regions adjoining stress fibers, where cortical actin was less dense and where microtubules displayed higher lateral fluctuations.

DISCUSSION

Our study provides the first experimental evidence that microtubule walls undergo self-repair in living cells. The negative correlation measured between the IT and ET intensities and the super-resolution imaging demonstrates that newly injected dimers are embedded in the microtubule lattice. Furthermore, the lower IT intensities in incorporations than microtubule tips discard the possibility of annealing between two microtubule growing ends. Finally, the saturation of IT intensities in incorporations, the saturation of the incorporation frequency as a function of concentration, and their preferential location in defined subcellular regions attest for the non-random binding of IT dimers in the pre-existing microtubule network. Altogether, our results attest the specificity of tubulin incorporations in limited number of sites in the microtubule lattice that are not randomly localized along microtubules. The preferential location of these sites in regions where microtubules displayed large lateral fluctuations and the saturation of the polymerization process strongly suggest that these incorporations are genuine repair sites where damaged lattice is healed by the addition of free dimers.

Interestingly, the ratio between the fluorescence intensity in incorporations and growing ends (Figure S2C) suggested that these incorporations contained between 4 and 8 repaired protofilaments. Smaller damages, in which only few protofilaments were repaired, might have been too dim to pass the fluorescence threshold we imposed (twice the background) to be counted as incorporation sites. On the contrary, it is possible that larger damages involving a higher number of protofilaments could not be repaired and rather triggered microtubule breakage and disassembly (Figure S1A). In any case, it is interesting to note that about half of the section of the microtubule could be

(D) Microtubule tips with polymerized IT were marked and analyzed along the microtubule filament, starting from the tip along a length of 1–1.5 μm. This length was then divided into regularly spaced 200-nm-thick line profiles perpendicular to the microtubule (white boxes). A total of 13 tips across 2 experiments from a total of 5 cells were analyzed, resulting in n = 100 line ROIs analyzed. Intensity profiles were calculated for IT and TT, aligned to the position of intensity maximum for TT (estimated using a Gaussian fit), and then averaged and plotted. Scale bars in all panels, 200 nm.

Please cite this article in press as: Gazzola et al., Microtubules self-repair in living cells, Current Biology (2022), https://doi.org/10.1016/j.cub.2022.11.060

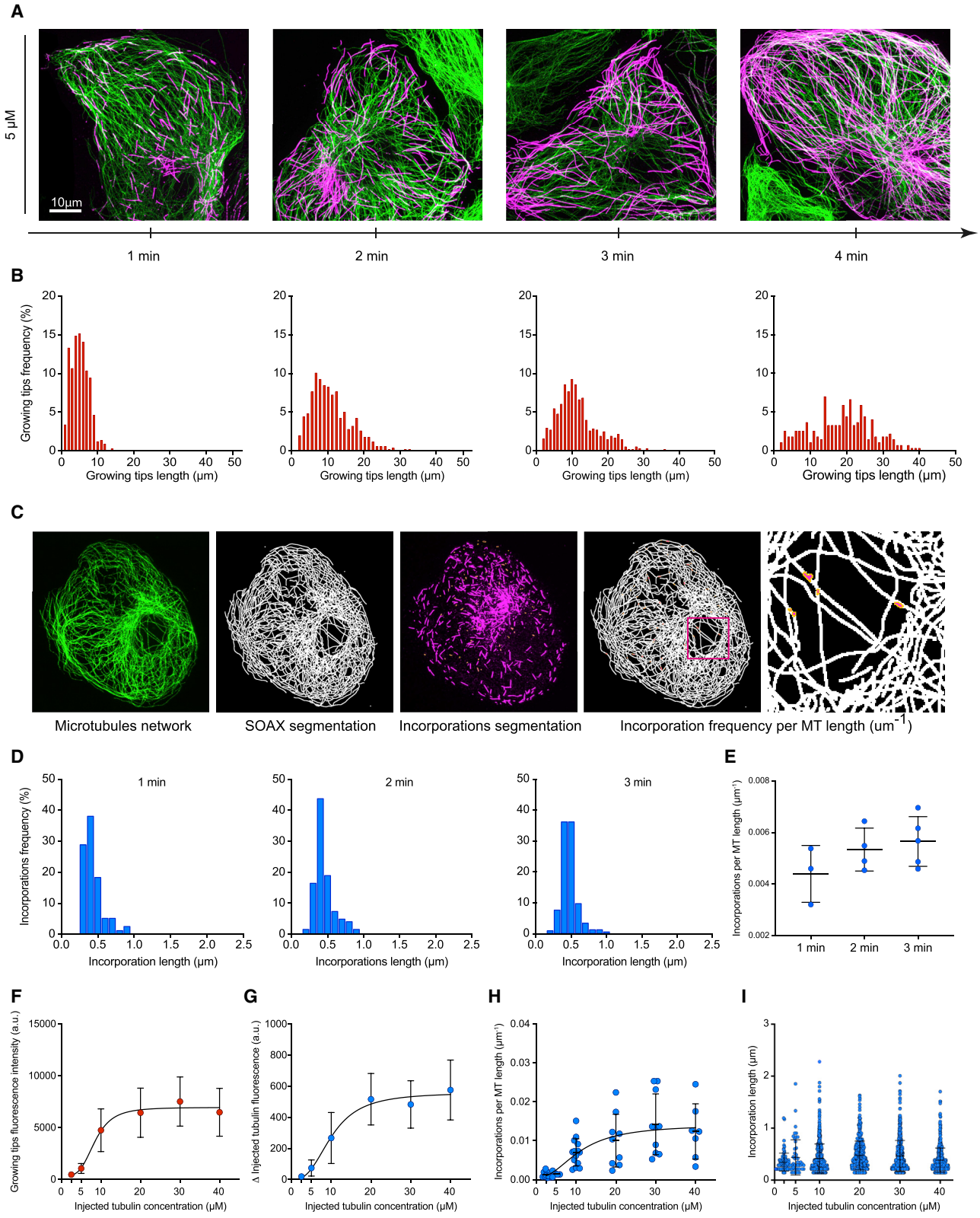

(legend on next page)

destroyed and repaired. This value is much larger than the low fluorescence intensity of incorporations observed along non-stabilized microtubules *in vitro* (1%–10% of lattice dimers).[10] It would be interesting to know more about the contribution of specific microtubule-associated proteins in the survival of such large damages and in the recruitment of new tubulin dimers to damaged sites. Also of interest is the possibility that such proteins heal the damage by stabilizing exposed ends of protofilaments and protect damage from disassembly without the need to incorporate for free dimers.[20] In both cases, it would be worth measuring the expression of those microtubule-associated proteins in specific cell types in which microtubules are more prone to be injured.

The value of one repair sites every 100 μm of microtubules (Figures 4E and 4H) is likely an underestimation of the actual spatial frequency of the repair sites. First, we considered only large damage sites in which IT fluorescence was twice higher than the background; hence, we discarded all the small repair involving few dimers. The high contrast of the STORM imaging revealed numerous small repairs whose intensities were close to the background and therefore ignored in all our quantifications. Second, the polymerization of IT at microtubule growing ends prevented us from looking at the repair process over duration longer than 4 min. Considering that microtubule's lifetime varies between 10 and 30 min, it is possible that the total number of incorporations during the entire lifetime of the microtubule is higher than our measurement. Finally, some repair sites may also have been protected by microtubule-associated proteins such as CLASP or SSNA1 without involving the incorporation of tubulin dimers.[17,20] Overall, the quantifications provided in this study report the spatial frequency of large damages in the lattice that have been repaired in a limited time window and involved dimer replacement. They likely largely underestimated the actual dynamics of the microtubule lattice.

Finally, we observed that incorporations were more frequent in regions adjoining stress fibers than in the lamella. It is counter-intuitive that the microtubules that were bent by the retrograde flow of the actin network in the lamella did not display more damages and repairs. It is possible that the characteristic timescale of actin retrograde flow (several dozen minutes) was too long to generate damages and repairs in the time window we analyzed (5 min). At this timescale, the actin network barely changed in the lamella (Figure 5C). The mechanism responsible for the incorporations we observed might operate at shorter timescales. Our investigation of microtubule network fluctuations, by monitoring microtubule shapes every 10 s during 5 min, revealed an interesting correlation with the spatial distribution of repair sites (Figures 5F and 5I). It is not yet known whether these fluctuations are at the origin of the microtubule damage or whether both phenomena are independent manifestations of the same originating mechanism. Indeed, molecular motors can both deform[37,38] and destroy microtubules.[19,39] In a nonexclusive mechanism, bending forces could also directly induce microtubule destruction and repair.[14] Whether and how the regulation of microtubule damage and repair has any impact on microtubule stability and cell polarity[21,25] is an interesting hypothesis that deserve further investigation.

Altogether, our results demonstrated that microtubules undergo frequent self-repair in living cells. They also revealed the existence of subcellular regulation mechanism that might contribute to determine specific populations of microtubules. The physiological impact of this destruction and repair mechanism remains to be determined.

STAR★METHODS

Detailed methods are provided in the online version of this paper and include the following:

- RESOURCE AVAILABILITY
  - Lead contact
  - Materials availability
  - Data and code availability
- EXPERIMENTAL MODEL AND SUBJECT DETAILS
  - Cell culture
- METHOD DETAILS
  - Tubulin purification and labelling
  - Microinjection
  - Cells fixation and labeling
  - Immunolabelling for STORM experiments
  - Imaging
  - STORM Imaging
  - Localization and image reconstruction
  - Micropatterning

Figure 4. Tubulin incorporation in the growing ends and in the lattice of pre-existing microtubules as a function of time and soluble tubulin concentration

(A) Incorporation of newly injected tubulin in the pre-existing microtubule network in PtK2 GFP-tubulin cells injected with 5 μM IT. Z acquisitions were performed and projected on a single image containing the maximal intensity of each pixel. Images show the newly incorporated tubulin in the microtubule network 1, 2, 3, and 4 min post-injection. Z acquisitions were performed and projected on a single image containing the maximal intensity of each pixel. Scale bars, 10 μm.

(B) Growing tips length distribution (in % of total growing tips) in cells injected with 5 μM IT 1, 2, 3, and 4 min post-injection.

(C) Workflow developed to measure the spatial frequency of incorporations in the microtubule network. The microtubule signal is segmented using SOAX[30] to measure the total length of the network. Incorporations are segmented manually.

(D) Incorporations length distribution (in % of total incorporations) in cells injected with 5 μM IT 1, 2, and 3 min post-injection.

(E) Incorporation frequency depending on the delay after microinjection of 5 μM tubulin. Data represent mean ± SD, n = 3–5 cells.

(F) IT fluorescence intensity measured at microtubule growing ends of cells injected with 2.5, 5, 10, 20, 30, and 40 μM IT. Data represent mean ± SD, n = 269–465 growing tips measured for at least 8 cells in each condition.

(G) Variations of IT intensity in incorporations as a function of IT concentration. Data represent mean ± SD, n = 9–15 from at least five cells for each condition.

(H) Incorporation frequency for various IT concentrations. Data represent mean ± SD, n = 5–14 analyzed cells in each condition in two independent experiments.

(I) Incorporation lengths for various IT concentrations. Data represent mean ± SD, n = 50–471 incorporations measured in each condition in two independent experiments.

See also Figures S3 and S4.

Please cite this article in press as: Gazzola et al., Microtubules self-repair in living cells, Current Biology (2022), https://doi.org/10.1016/j.cub.2022.11.060

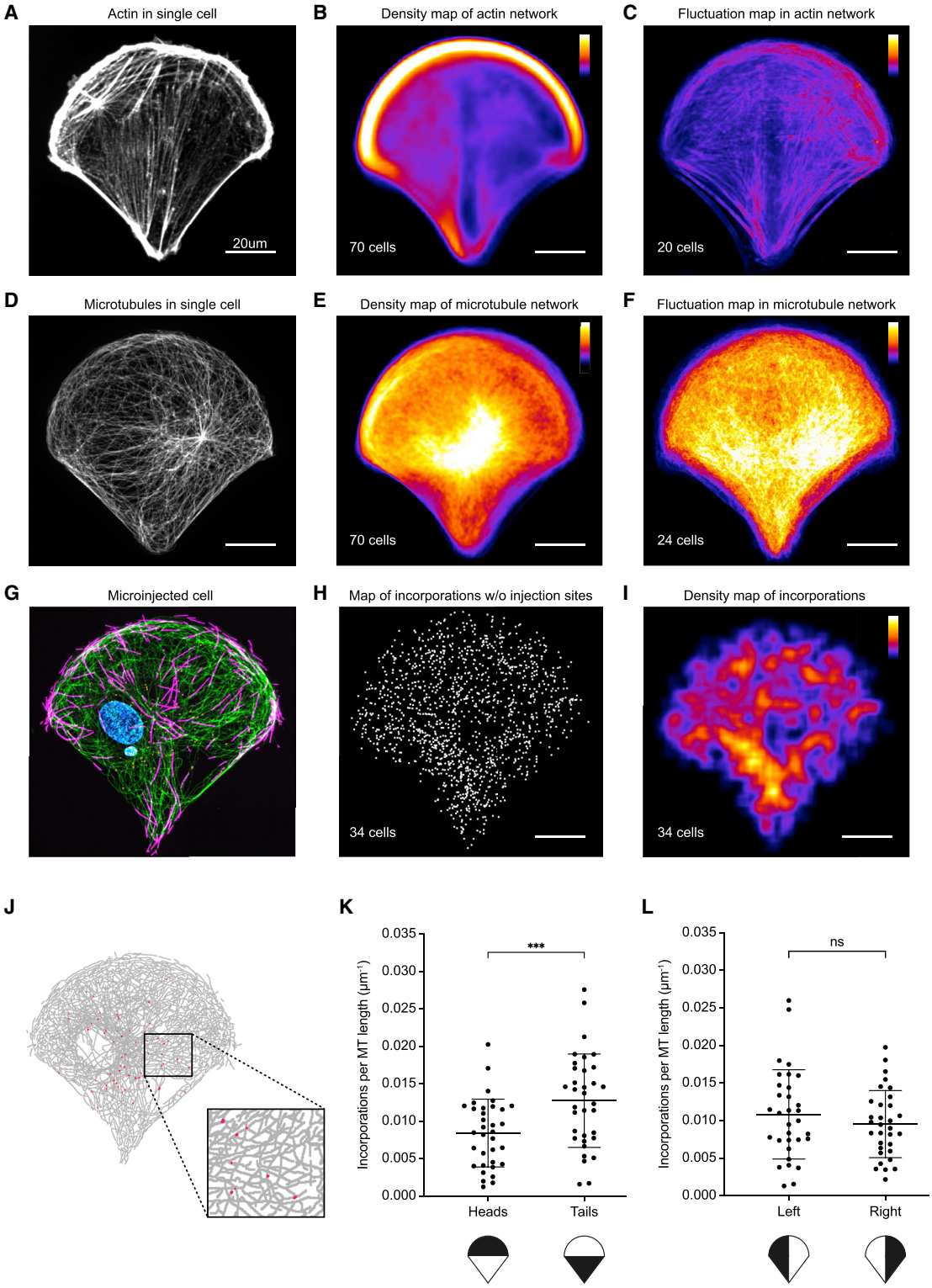

Figure 5. Distribution of repair sites in micropatterned PtK2 cells

(A) Representative image of the actin network in PtK2 GFP-tubulin cell plated on a crossbow-shape fibronectin-coated micropattern. Z acquisitions were performed and projected on a single image containing the maximal intensity of each pixel. Scale bars, 20 µm.

(B) Averaged fluorescence signal of F-actin of 70 images. Intensities are color coded with the "fire" look-up table. Scale bars, 20 µm.

(legend continued on next page)

- QUANTIFICATION AND STATISTICAL ANALYSIS
  - Average linescan profiles for STORM analysis

SUPPLEMENTAL INFORMATION

Supplemental information can be found online at https://doi.org/10.1016/j.cub.2022.11.060.

ACKNOWLEDGMENTS

This work was supported by the European Research Council (Consolidator Grant 771599 [ICEBERG] to M.T. and Advanced Grant 741773 [AAA] to L.B.), the Bettencourt-Schueller Foundation, the Emergence program of the Ville de Paris, and the Schlumberger Foundation for Education and Research. This project was also supported by the MuLife imaging facility, which is funded by GRAL, a program from the Chemistry Biology Health Graduate School of University Grenoble Alpes (ANR-17-EURE-0003).

AUTHOR CONTRIBUTIONS

Conceptualization, A.S., C.L., L.B., M.G., and M.T.; funding acquisition, C.L., L.B., and M.T.; methodology, A.S., B.V., C.L., J.G., and M.G.; investigation, A.S., C.B.-H., K.F., and M.G.; analysis, A.S., C.B.-H., C.L., L.B., M.G., and M.T.; supervision, C.L., L.B., and M.T.; writing, L.B., M.G., and M.T.

DECLARATION OF INTERESTS

Karoline Friedl works for Abbelight, whose products were used for STORM imaging and described in the STAR Methods section.

Received: April 11, 2022
Revised: September 21, 2022
Accepted: November 24, 2022
Published: December 23, 2022

REFERENCES

1. Akhmanova, A., and Kapitein, L.C. (2022). Mechanisms of microtubule organization in differentiated animal cells. Nat. Rev. Mol. Cell Biol. *23*, 541–558.
2. Nogales, E., and Zhang, R. (2016). Visualizing microtubule structural transitions and interactions with associated proteins. Curr. Opin. Struct. Biol. *37*, 90–96.
3. Wade, R.H., and Chrétien, D. (1993). Cryoelectron microscopy of microtubules. J. Struct. Biol. *110*, 1–27.
4. Brouhard, G.J., and Rice, L.M. (2018). Microtubule dynamics: an interplay of biochemistry and mechanics. Nat. Rev. Mol. Cell Biol. *19*, 451–463.
5. Cleary, J.M., and Hancock, W.O. (2021). Molecular mechanisms underlying microtubule growth dynamics. Curr. Biol. *31*, R560–R573.
6. Akhmanova, A., and Steinmetz, M.O. (2015). Control of microtubule organization and dynamics: two ends in the limelight. Nat. Rev. Mol. Cell Biol. *16*, 711–726.
7. Cross, R.A. (2019). Microtubule lattice plasticity. Curr. Opin. Cell Biol. *56*, 88–93.
8. Théry, M., and Blanchoin, L. (2021). Microtubule self-repair. Curr. Opin. Cell Biol. *68*, 144–154.
9. Dye, R.B., Flicker, P.F., Lien, D.Y., and Williams, R.C. (1992). End-stabilized microtubules observed in vitro: stability, subunit, interchange, and breakage. Cell Motil. Cytoskeleton *21*, 171–186.
10. Schaedel, L., Triclin, S., Chrétien, D., Abrieu, A., Aumeier, C., Gaillard, J., Blanchoin, L., Théry, M., and John, K. (2019). Lattice defects induce microtubule self-renewal. Nat. Phys. *15*, 830–838.
11. Chrétien, D., and Fuller, S.D. (2000). Microtubules switch occasionally into unfavorable configurations during elongation. J. Mol. Biol. *298*, 663–676.
12. Chretien, D., Metoz, F., Verde, F., Karsenti, E., and Wade, R.H. (1992). Lattice defects in microtubules: protofilament numbers vary within individual microtubules. J. Cell Biol. *117*, 1031–1040.
13. Guyomar, C., Bousquet, C., Ku, S., Heumann, J., Guilloux, G., Gaillard, N., Heichette, C., Duchesne, L., Steinmetz, M.O., Gibeaux, R., et al. (2022). Changes in seam number and location induce holes within microtubules assembled from porcine brain tubulin and in *Xenopus* egg cytoplasmic extracts. Preprint at bioRxiv. https://doi.org/10.1101/2021.07.14.452321.
14. Schaedel, L., John, K., Gaillard, J.J., Nachury, M.V.M.V., Blanchoin, L., Théry, M., and Thery, M. (2015). Microtubules self-repair in response to mechanical stress. Nat. Mater. *14*, 1156–1163.
15. Reid, T.A., Coombes, C., and Gardner, M.K. (2017). Manipulation and quantification of microtubule lattice integrity. Biol. Open *6*, 1245–1256.
16. Vemu, A., Szczesna, E., Zehr, E.A., Spector, J.O., Grigorieff, N., Deaconescu, A.M., and Roll-Mecak, A. (2018). Severing enzymes amplify microtubule arrays through lattice GTP-tubulin incorporation. Science *361*, eaau1504.
17. Lawrence, E.J., Arpag, G., Arnaiz, C., and Zanic, M. (2021). Ssna1 stabilizes dynamic microtubules and detects microtubule damage. eLife *10*, 1–21.
18. Goldblum, R.R., McClellan, M., White, K., Gonzalez, S.J., Thompson, B.R., Vang, H.X., Cohen, H., Higgins, L.A., Markowski, T.W., Yang, T.Y., et al. (2021). Oxidative stress pathogenically remodels the cardiac myocyte cytoskeleton via structural alterations to the microtubule lattice. Dev. Cell *56*, 2252–2266.e6.

(C) Averaged fluctuations of actin signal reporting the subcellular regions where actin bundles move. Actin signal was measured every 4 s for 3 min. The standard deviation of the signal was measured for each individual cells and averaged over n = 20 cells. Intensities were color coded with the fire look-up table. Scale bars, 20 μm.
(D) Representative image of the microtubule network in the PtK2 GFP-tubulin cell. Z acquisitions were performed and projected on a single image containing the maximal intensity of each pixel. Scale bars, 20 μm.
(E) Averaged fluorescence signal of microtubules (GFP signal) of 70 images. Intensities are color coded with the fire look-up table. Scale bars, 20 μm.
(F) Averaged fluctuations of tubulin signal reporting regions where microtubules move. Tubulin signal was measured every 10 s for 3 min. The standard deviation of the signal was measured for each individual cells and averaged over n = 20 cells. Intensities were color coded with the fire look-up table. Scale bars, 10 μm.
(G) Representative image of a PtK2 GFP-tubulin (green) cell microinjected with 20 μM ATTO-565 tubulin (magenta). Z acquisitions were performed and projected on a single image containing the maximal intensity of each pixel. Scale bars, 20 μm.
(H) Overlay of the positions of incorporations measured in 34 cells from six independent experiments after the removal of incorporations close to the injection site. Scale bars, 20 μm.
(I) Density map of incorporations measured in (H). The distribution of positions was spatially averaged using a 40-pixel-wide sliding square and color coded with the fire look-up table. Scale bars, 20 μm.
(J) Representative image of a SOAX segmented microtubule network (gray) containing IT incorporations (red) in a PtK2 GFP-tubulin cell micropatterned on a crossbow shape.
(K) Spatial frequency of incorporations measured in the top and bottom part of PtK2 cells micropatterned on crossbow shapes. Data represent mean ± SD, n = 34 cells from six individual experiments. Statistical analysis was performed using two-tailed paired t test, ***p = 0.0005.
(L) Same as (K) but measurements were performed in the left and right parts of the cells.
See also Figures S4 and S5 and Videos S2, S3, and S4.

19. Triclin, S., Inoue, D., Gaillard, J., Htet, Z.M., DeSantis, M.E., Portran, D., Derivery, E., Aumeier, C., Schaedel, L., John, K., et al. (2021). Self-repair protects microtubules from destruction by molecular motors. Nat. Mater. *20*, 883–891.

20. Aher, A., Rai, D., Schaedel, L., Gaillard, J.J., John, K., Liu, Q., Altelaar, M., Blanchoin, L., Thery, M., and Akhmanova, A. (2020). CLASP mediates microtubule repair by restricting lattice damage and regulating tubulin incorporation. Curr. Biol. *30*, 2175–2183.e6.

21. Aumeier, C., Schaedel, L., Gaillard, J., John, K., Blanchoin, L., and Théry, M. (2016). Self-repair promotes microtubule rescue. Nat. Cell Biol. *18*, 1054–1064.

22. Chakraborty, S., Mahamid, J., and Baumeister, W. (2020). Cryoelectron tomography reveals nanoscale organization of the cytoskeleton and its relation to microtubule curvature inside cells. Structure *28*, 991–1003.e4.

23. Atherton, J., Stouffer, M., Francis, F., and Moores, C.A. (2018). Microtubule architecture in vitro and in cells revealed by cryo-electron tomography. Acta Crystallogr. D Struct. Biol. *74*, 572–584.

24. Atherton, J., Stouffer, M., Francis, F., and Moores, C.A. (2022). Visualising the cytoskeletal machinery in neuronal growth cones using cryo-electron tomography. J. Cell Sci. *135*, jcs259234.

25. Andreu-Carbó, M., Fernandes, S., Velluz, M.-C., Kruse, K., and Aumeier, C. (2022). Motor usage imprints microtubule stability along the shaft. Dev. Cell *57*, 5–18.e8.

26. Nihongaki, Y., Matsubayashi, H.T., and Inoue, T. (2021). A molecular trap inside microtubules probes luminal access by soluble proteins. Nat. Chem. Biol. *17*, 888–895.

27. Dimitrov, A., Quesnoit, M., Moutel, S., Cantaloube, I., Poüs, C., and Perez, F. (2008). Detection of GTP-tubulin conformation in vivo reveals a role for GTP remnants in microtubule rescues. Science *322*, 1353–1356.

28. de Forges, H., Pilon, A., Cantaloube, I., Pallandre, A., Haghiri-Gosnet, A.-M.M., Perez, F., and Poüs, C. (2016). Localized mechanical stress promotes microtubule rescue. Curr. Biol. *26*, 3399–3406.

29. Schulze, E., and Kirschner, M.W. (1986). Microtubule dynamics in interphase cells. J. Cell Biol. *102*, 1020–1031.

30. Schulze, E., and Kirschner, M.W. (1987). Dynamic and stable populations of microtubules in cells. J. Cell Biol. *104*, 277–288.

31. Amann, K.J., and Pollard, T.D. (2001). Direct real-time observation of actin filament branching mediated by Arp2/3 complex using total internal reflection fluorescence microscopy. Proc. Natl. Acad. Sci. USA *98*, 15009–15013.

32. Molines, A.T., Lemière, J., Gazzola, M., Steinmark, I.E., Edrington, C.H., Hsu, C.T., Real-Calderon, P., Suhling, K., Goshima, G., Holt, L.J., et al. (2022). Physical properties of the cytoplasm modulate the rates of microtubule polymerization and depolymerization. Dev. Cell *57*, 466–479.e6.

33. Xu, T., Vavylonis, D., Tsai, F.-C., Koenderink, G.H., Nie, W., Yusuf, E., Lee, I.-J., Wu, J.-Q., and Huang, X. (2015). SOAX: a software for quantification of 3D biopolymer networks. Sci. Rep. *5*, 9081.

34. Portran, D., Schaedel, L., Xu, Z., Théry, M., and Nachury, M.V. (2017). Tubulin acetylation protects long-lived microtubules against mechanical ageing. Nat. Cell Biol. *19*, 391–398.

35. Théry, M., Racine, V., Piel, M., Pépin, A., Dimitrov, A., Chen, Y., Sibarita, J.-B., and Bornens, M. (2006). Anisotropy of cell adhesive microenvironment governs cell internal organization and orientation of polarity. Proc. Natl. Acad. Sci. USA *103*, 19771–19776.

36. Katrukha, E.A., Mikhaylova, M., van Brakel, H.X., van Bergen en Henegouwen, P.M., Akhmanova, A., Hoogenraad, C.C., and Kapitein, L.C. (2017). Probing cytoskeletal modulation of passive and active intracellular dynamics using nanobody-functionalized quantum dots. Nat. Commun. *8*, 14772.

37. Jolly, A.L., Kim, H., Srinivasan, D., Lakonishok, M., Larson, A.G., and Gelfand, V.I. (2010). Kinesin-1 heavy chain mediates microtubule sliding to drive changes in cell shape. Proc. Natl. Acad. Sci. USA *107*, 12151–12156.

38. Randall, T.S., Yip, Y.Y., Wallock-Richards, D.J., Pfisterer, K., Sanger, A., and Ficek, W. (2017). A small-molecule activator of kinesin-1 drives remodeling of the microtubule network. Proc. Natl. Acad. Sci. USA *114*, 13738–13743.

39. Budaitis, B.G., Badieyan, S., Yue, Y., Blasius, T.L., Reinemann, D.N., Lang, M.J., Cianfrocco, M.A., and Verhey, K.J. (2022). A kinesin-1 variant reveals motor-induced microtubule damage in cells. Curr. Biol. *32*, 2416–2429.e6.

40. Edelstein, A., Amodaj, N., Hoover, K., Vale, R., and Stuurman, N. (2010). Computer control of microscopes using μManager. Curr. Protoc. Mol. Biol. *92*, 14.20.1–14.20.17.

41. Rueden, C.T., Schindelin, J., Hiner, M.C., DeZonia, B.E., Walter, A.E., Arena, E.T., and Eliceiri, K.W. (2017). ImageJ2: ImageJ for the next generation of scientific image data. BMC Bioinformatics *18*, 529.

42. Shelanski, M.L. (1973). Chemistry of the filaments and tubules of brain. J. Histochem. Cytochem. *21*, 529–539.

43. Hyman, A., Drechsel, D., Kellogg, D., Salser, S., Sawin, K., Steffen, P., Wordeman, L., and Mitchison, T. (1991). Preparation of modified tubulins. Methods Enzymol. *196*, 478–485.

44. Vantard, M., Peter, C., Fellous, A., Schellenbaum, P., and Lambert, A.M. (1994). Characterization of a 100-kDa heat-stable microtubule-associated protein from higher plants. Eur. J. Biochem. *220*, 847–853.

45. Mau, A., Friedl, K., Leterrier, C., Bourg, N., and Lévêque-Fort, S. (2021). Fast widefield scan provides tunable and uniform illumination optimizing super-resolution microscopy on large fields. Nat. Commun. *12*, 3077.

46. Thevathasan, J.V., Kahnwald, M., Cieśliński, K., Hoess, P., Peneti, S.K., Reitberger, M., Heid, D., Kasuba, K.C., Hoerner, S.J., Li, Y., et al. (2019). Nuclear pores as versatile reference standards for quantitative superresolution microscopy. Nat. Methods *16*, 1045–1053.

47. Ovesný, M., Křížek, P., Borkovec, J., Švindrych, Z., and Hagen, G.M. (2014). ThunderSTORM: a comprehensive ImageJ plug-in for PALM and STORM data analysis and super-resolution imaging. Bioinformatics *30*, 2389–2390.

Please cite this article in press as: Gazzola et al., Microtubules self-repair in living cells, Current Biology (2022), https://doi.org/10.1016/j.cub.2022.11.060

STAR★METHODS

REAGENT or RESOURCE	SOURCE	IDENTIFIER
Antibodies		
ATTO-565	Sigma	75784
Phalloidin-A555	Life Technologies	A34055
Anti-alpha tubulin DM1A	Abcam	Abcam Cat# ab7291; RRID: AB_2241126
Sir-Actin	Cytoskeleton	CY-SC001
Anti-alpha tubulin B512	Sigma	Sigma-Aldrich Cat# T5168; RRID: AB_477579
Goat anti-Mouse CF680	Biotium	Biotium Cat# 20273-2; RRID: AB_10852849
Chemicals, peptides, and recombinant proteins		
Paraformaldehyde	Euromedex	15710
Glutaraldehyde	Sigma	G5882
Fibronectin	Sigma	F1141
PLL(20)-g[3.5]-PEG(2)	SurfaceSolutionS	PLL(20)-g[3.5]-PEG(2)
Collagen I Rat Protein	GIBCO	A1048301
Experimental models: Cell lines		
PtK2 cell line stably expressing GFP-tubulin	Franck Perez Lab	Dimitrov et al.[27]
Software and algorithms		
Metamorph	Molecular Devices	https://www.moleculardevices.com/products/cellular-imaging-systems/acquisition-and-analysis-software/metamorph-microscopy
MicroManager	micro-manager.org	Edelstein et al.[40]
ImageJ	http://imageJ.nih.gov/ij	Rueden et al.[41]
SOAX	https://www.lehigh.edu/~div206/soax/	Xu et al.[33]
Prism 9	GraphPad Software	https://www.graphpad.com/scientific-software/prism/
Other		
Inverted spinning disk microscope Nikon TiE equipped with a Retiga R3 camera (Photometrics), a spinning scanning unit CSU-X1 Yokogawa and a motorized stage.	Nikon, Hamamatsu, Märzhäuser	Gattaca for custom configuration of microscope set-up
Inverted microscope Nikon Ti2 equipped with a InjectMan 4 micromanipulator and a Prime BSI Express CMOS camera.	Nikon, Eppendorf, Okolab, Photometrics	Nikon for custom configuration of microscope set-up
Air-plasma	Plasma Etch	PE-30
Photomask	Toppan Photomask	Quartz grade D (MFS > 1mm)
borosilicate thin wall capillary	Harvard Apparatus	30-0050
Pipette puller	Narishige	PN-3
Abbelight Smart Buffer	Abbelight	N/A

RESOURCE AVAILABILITY

Lead contact

Further information and requests for resources and reagents should be directed to and will be fulfilled by the Lead Contact, Manuel Théry (manuel.thery@cea.fr).

Materials availability

This study did not generate new unique reagents. All materials generated for this study are available upon request.

Data and code availability

- The datasets supporting the current study have not been deposited in a public repository but are available from the corresponding or the first author on request.
- Custom Fiji scripts and macros to translate coordinate files and automate image reconstruction for whole images at 16 nm/pixel and detailed zooms on IT integration regions at 4 nm/pixel are available at https://github.com/cleterrier/ChriSTORM. The ProFeat script for the generation of linescan profiles and CrossAlign profiles script to align all linescans are both available at https://github.com/cleterrier/Measure_ROIs. Any additional information required to reanalyze the data reported on this paper is available from the lead contact upon request.
- The SOAX software is available in the following link: https://www.lehigh.edu/~div206/soax

EXPERIMENTAL MODEL AND SUBJECT DETAILS

Cell culture

Male rat kangaroo kidney epithelial cells (PtK2) stably expressing GFP-Tubulin obtained from Franck Perez lab were grown at 37°C and 5% CO_2 in DMEM/F12 (31331028, Gibco) supplemented with 10% fetal bovine serum (10270106, Life Technologies) and 1% antibiotic-antimycotic solution (15240062, Gibco). The information of the sexe or the developmental stage from which the cells were extracted is not available. The day before experiments, cells were detached using TrypLE (12605036, GIBCO) and plated in glass bottom dish (627860, Dutscher) or in micropatterned coverslips glued to home-made cut out plastic dish.

METHOD DETAILS

Tubulin purification and labelling

Fluorescent tubulin (ATTO-565-labelled tubulin) were prepared as previously described.[42–44] Briefly, tubulin was purified from fresh bovine brain by three cycles of temperature-dependent assembly and disassembly in Brinkley buffer 80 (BRB80 buffer: 80mM PIPES pH 6.8, 1mM EGTA and 1mM MgCl2 plus 1mM GTP). MAP-free neurotubulin was purified by cation-exchange chromatography (EMDSO, 650M, Merck) in 50mM PIPES, pH 6.8, supplemented with 1mM MgCl2 and 1mM EGTA. Purified tubulin was obtained after a cycle of polymerization and depolymerization. Finally, tubulin was labelled with ATTO-565 fluorochromes, resuspended in microinjection buffer (50 mM potassium glutamate, 1 mM MgCl2, pH 6.8), aliquoted in 500μl plastic tubes, flash frozen in liquid nitrogen and store at -80°C.

Microinjection

Glass microneedles were home-made pulled from clark borosilicate thin wall capillary (30-0050 Harvard Apparatus) using a horizontal pipet puller (PN-3, Narishige). Purified labelled tubulin was thaw and diluted in injection buffer (50 mM potassium glutamate, 1 mM MgCl2, pH 6.8) on ice to reach final concentration. Microneedles were loaded with 5μL of tubulin solution and connected to a FemtoJet 4i (Eppendorf). Microneedles were manually controlled with an InjectMan 4 micromanipulator (Eppendorf). The compensation pressure set on the FemtoJet was 35hPa for the whole injection experiment to avoid damages on cells. Microinjection of PTK2 cells were performed in an inverted microscope (Nikon Ti2 Eclipse) equipped with a Prime BSI Express CMOS camera (Photometrics) and using a Nikon CFI Plan Fluor 40x/0.75 NA dry objective. Cell medium was maintained at 37°C and 5% CO2 during the whole experiment using a H-301 heating chamber (Okolab). Micro-Manager 1.4.21 software was used for images acquisition.

Cells fixation and labeling

Before fixation, cells were permeabilized with BRB80 1X supplemented with 0.25% Triton-X100 (T8787, Sigma) for 30 sec, and then fixed in cytoskeleton buffer (MES 10mM, KCl 138mM, MgCl 3mM, EGTA 2mM) supplemented with 10% sucrose, 0.5% Triton-X100 and 0.5% glutaraldehyde (G5882, Sigma). Aldehyde functions were then reduced using 1mg/ml of $NaBH_4$ for 10 minutes at room temperature. Cells were washed 3 times with PBS-Tween 20 (1379, Sigma) 0.1% and incubated with phalloidin for 30 min and DAPI (D9542, Sigma) for 5 minutes. Coverslips were finally washed 3 times in PBS-Tween 20 0.1% and mounted in Mowiol 4-88 (81381, Sigma).

Immunolabelling for STORM experiments

Samples were first rinsed three times with TpO4 (phosphate buffer 0.1 M pH 7.4) and then blocked with TPT (TpO4, gelatin 0.22%, TritonX-100 0.1%) for 2 hours at room temperature on a shaker inside a dark chamber. For visualization of total tubulin two mouse anti-α tubulin antibodies were diluted in TpT and incubated overnight at +4°C. After 3 washes with TpT for 10 minutes, each sample was incubated with anti-mouse CF680 secondary antibody for 60 minutes at room temperature then rinsed with TpT followed by 2 TpT washes of 10 minutes and 2 TpO4 washes of 10 minutes. Samples were stored in TP04 with 0.02% NaN_3 at +4°C when not imaged.

Imaging

Immunofluorescence images of GFP microtubules and injected ATTO-565-tubulin in cells were acquired using a confocal spinning disk microscope (Nikon Ti Eclipse equipped with a spinning scanning unit CSU-X1 Yokogawa) and a R3 retiga camera (QImaging). Images were acquired using a Nikon Plan Apo VC 60x/1.40 NA oil objective using a 1.5x additional integrated magnification lens. Each wavelength was acquired separately with a 200nm Z-step width. Metamorph software was used for images acquisition.

STORM Imaging

For multicolor SMLM, we used Stochastic Optical Microscopy (STORM) with spectral unmixing. STORM was performed on a dual-view SAFe360 module (Abbelight), mounted to a Nikon inverted Ti2 stand with a 100X NA 1.49 objective. The SAFe360 system includes an L4Cc Oxxius laser combiner with four laser lines of which we used a 640 nm (500 mW) for excitation and a 405 nm line (100 mW) to recover fluorophores from a long live dark state. Excitation was performed in HiLo configuration and with ASTER scanning.[45] The fluorescent signal was filtered by an excitation light filtering quad-band dichroic mirror (Semrock, Di03-R405/488/532/635-t3-25x36), split with a 700 nm dichroic mirror (Semrock, FF699-FDi01-t3-25x36), and subsequently detected on two ORCA-Flash4.0 V3 Digital sCMOS cameras (Hamamatsu Photonics). The inner well of glass-bottom dishes was filled with STORM buffer (Smart Buffer Kit, Abbelight) and sealed with a glass coverslip. After locating a microinjected cell using low-intensity illumination a STORM acquisition was captured. 30,000-60,000 images (1024x1024 or 512x512 pixels, 15-50 ms exposure time) were acquired at full 640 nm laser power. Reactivation of fluorophores was performed manually during the acquisition by increasing illumination with the 405 nm laser (power and maximum of 20%).

Localization and image reconstruction

Neo Analysis software v38.9 (Abbelight) was used for detection and localization of single fluorophore activations from the TIFF files. First, background was removed by subtraction of local means and a standard intensity threshold of 1 or for low intensity a threshold of 0.5 was set where peaks above the determined intensity threshold were fitted to a Gaussian function by nonlinear least-square fitting. Peaks detected in successive frames at a maximum distance of 100 nm were considered as originating from a single activation burst and grouped. The localization text files created from each camera were then processed to detect blinking events on both cameras and pair them. The intensity of those pairs was counted over an area of 11x11 pixels, and a ratio calculated using

$$r = \frac{I_{trans}}{I_{trans} + I_{ref}}$$

Where I_{trans} is transmitted emission and I_{ref} is reflected photons. The localisations were then associated with a fluorophore by using ratios 0-0.42 for AF647-IT and 0.44-1 for CF680-TT and exported as channel-specific text files. Pairs of channel-specific files were then drift corrected using redundant cross-correlation in SMAP software.[45] Uncertainty was scaled by a factor of 0.4 to compensate for gaussian reconstruction blurring[46] and localizations above 12 nm of uncertainty (sigma) were filtered out. Gaussian image reconstructions with individual localization uncertainties were performed using the ThunderSTORM ImageJ plugin[47] in Fiji software. Custom scripts and macros were used to translate coordinate files, as well as automate images reconstruction for whole images at 16 nm/pixel and detailed zooms on IT integration regions at 4 nm/pixel (https://github.com/cleterrier/ChriSTORM).

Micropatterning

Clean glass coverslips were activated with an oxygen plasma treatment (PE50 - PlasmaEtch) for 30s at 30W and incubated with 0.1 mg/ml of poly(L-Lysine)-poly(ethylene-glycol) (PLL-PEG JenKem Technology) in 10 mM Hepes, pH 7.4, at room temperature for 1 h. Coverslips were then dried following dewetting in the presence of 1ml of ultra-pure H_2O. PLL-PEG coated coverslips were placed in contact with an optical mask containing transparent micropatterns (Toppan Photomasks, Inc.) using a home-made vacuum chamber and exposed for 4 min to deep UV light (UVO Cleaner 42; Jelight Company). Micropatterned slides were finally incubated for 20 min with a solution of 10 μg/ml bovine fibronectin solution (F1141, Sigma) and 10 μg/ml of Collagen I Rat Protein, Tail (A1048301, GIBCO) in $NaHCO_3$ 10mM. Before plating cells, patterned coverslips were washed one time with $NaHCO_3$ followed by three washes with ultra-pure H_2O.

QUANTIFICATION AND STATISTICAL ANALYSIS

All the statistical analysis has been performed using the Prism software (version 9). All the statistical information regarding tests, analyses, exact values of N, dispersions and precise measures can be found in figure legends. Acquired images were analyzed using ImageJ. In the red channel of acquired images (corresponding to the injected tubulin), 3 squares at different cell locations were chosen to measure the mean fluorescent intensity of the background. Red signal not corresponding to growing tips, and above 2 time the background signal on microtubule were manually selected as incorporations (Figure S1B). The total microtubule length was obtained using the SOAX software.[33] Finally, the incorporation frequency was measured by dividing the number of incorporations on the total length of the microtubule network. For the density maps, actin and microtubules images were aligned using the StackReg plugin in imageJ, projected on a single image containing the average intensity of each pixel and intensities were color coded with the "fire" look-up table. For the fluctuation maps, the background of the actin and microtubule images was subtracted, and they were equalized for the dynamic ranges of grey values. The standard deviations of each film were then stacked, aligned using StackReg plugin in

imageJ, and projected on a single image containing the average intensity of each pixel. The intensities were color coded with the 'fire'' look-up table. Statistical analysis was performed using GraphPad Prism software (version 9.0), a p-value above 0.05 was consider as significant.

Average linescan profiles for STORM analysis

Average linescan profiles were used to measure the width of IT integration sites along the microtubule lattice and at polymerizing microtubule tips. STORM data with a standard threshold detection of localization (1.0) for higher precision was used to create detailed zooms with 4nm/pixel. To investigate repair sites, we examined microtubules without IT containing polymerized tips. Repair sites across 2 experiments from a total of 5 cells were analyzed using a 200 nm-thick line profile drawn perpendicular to the microtubule with a total of n=100 line ROIs analyzed. Linescan profiles were generated using the Fiji script ProFeatFit to measure intensity profiles for IT and TT, which were then aligned to the position of intensity maximum for TT (estimated using a Gaussian fit) using a CrossAlign profiles script (https://github.com/cleterrier/Measure_ROIs). Plots were then grouped in GraphPad Prism 9 to generate an average linescan profile for repair sites.

Microtubule tips with polymerized IT were marked starting from the tip to a length of 1-1.5μm down the microtubule lattice. This length was then divided into regularly-spaced 200 nm-thick line profiles perpendicular to the microtubule. A total of 13 tips across 2 experiments from a total of 5 cells were analyzed, resulting in n=100 line ROIs analyzed. Similar to repairs, microtubule tip linescan profiles were generated in Fiji and an average linescan profile was plotted in Graphpad Prism 9.

Current Biology, Volume *33*

Supplemental Information

Microtubules self-repair in living cells

Morgan Gazzola, Alexandre Schaeffer, Ciarán Butler-Hallissey, Karoline Friedl, Benoit Vianay, Jérémie Gaillard, Christophe Leterrier, Laurent Blanchoin, and Manuel Théry

A

Linear incorporations

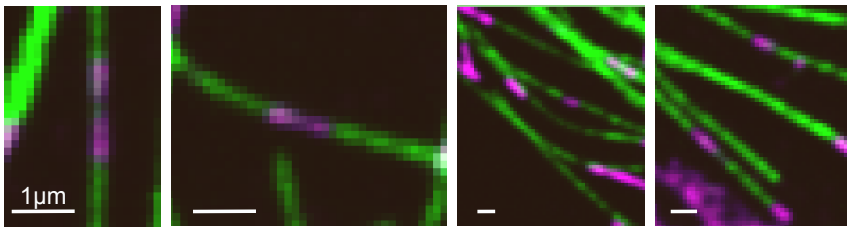

Incorporations in curved regions

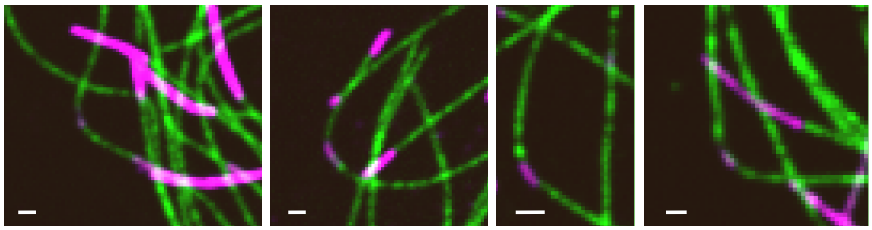

Incorporations near crossover sites

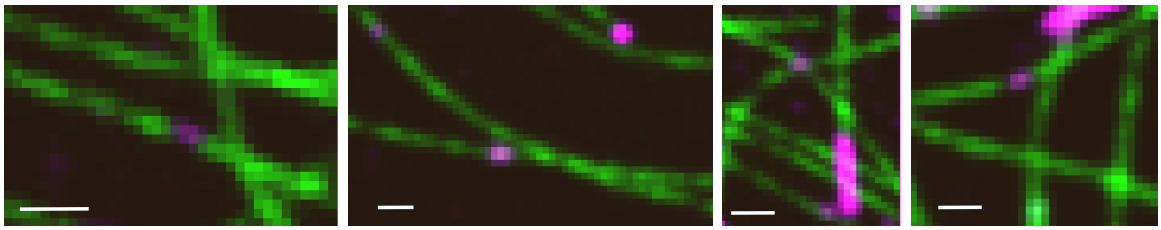

Kinked incorporations

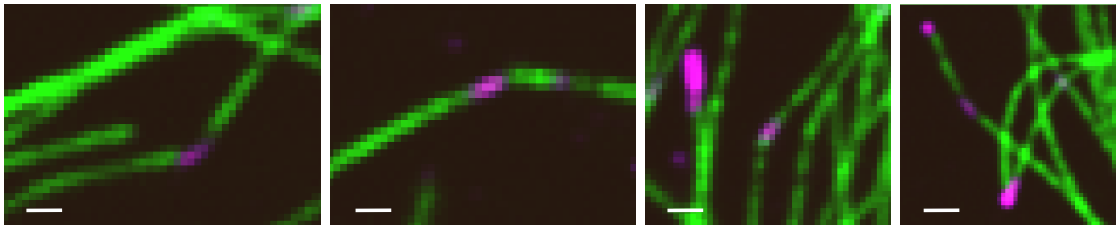

Broken incorporations

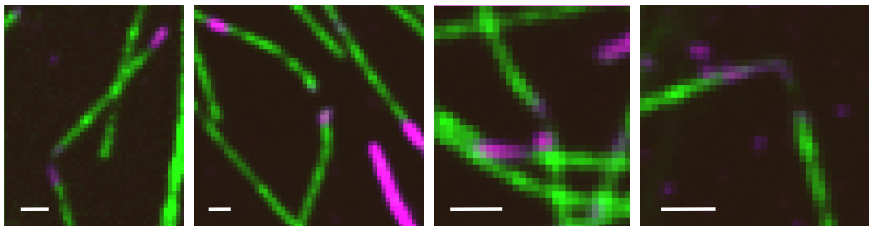

B

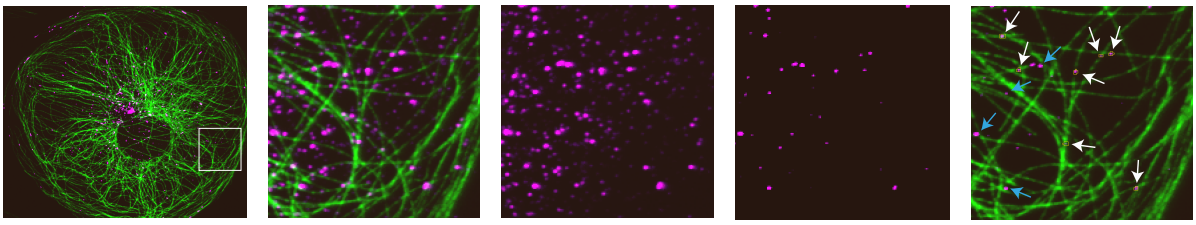

Figure S1: Bestiary of incorporations observed in PtK2 cells, Related to Figure 1.

(**A**) Different kind of incorporations observed in cells injected with concentration of IT ranging from 5 to 30 µM. Z acquisitions were performed and projected on a single image containing the sum intensity of each pixel. Scale bar, 1 µm. (**B**) Workflow developed to manually segment incorporations with a signal at least twice as high as the background noise.

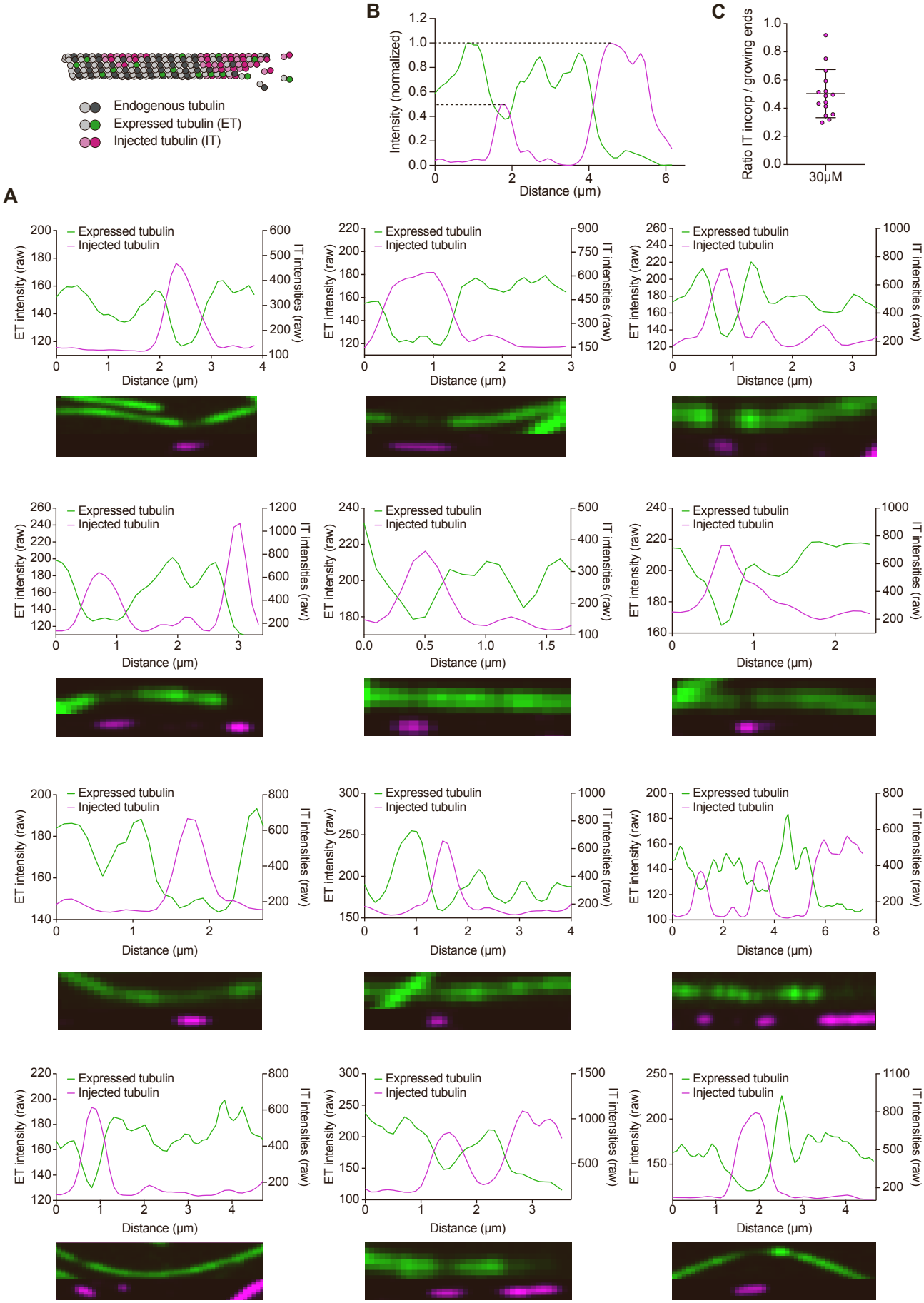
Endogenous tubulin
Expressed tubulin (ET)
Injected tubulin (IT)
B
Intensity (normalized)
Distance (µm)
C
Ratio IT incorp / growing ends
30µM
A
Expressed tubulin
Injected tubulin
ET intensity (raw)
IT intensities (raw)
Distance (µm)

Figure S2: Examples of anti-correlation between injected tubulin patches and fluorescence decrease of pre-existing lattice, Related to Figure 2.

(**A**) Fluorescence intensity profiles of microtubules exhibiting a patch of IT. Corresponding fluorescence images of expressed tubulin (ET) and injected tubulin (IT) are shown in green and magenta, respectively. (**B**) Representative fluorescence intensity profiles of microtubules exhibiting a patch of IT. Profiles have been normalized to 1 for the shaft signal of ET and for the peak of IT. (**C**) IT-fluorescence intensity ratios between the maximum intensity measured in the patches and the maximum intensity measured at the growing ends in PtK2 GFP-tubulin cells microinjected with 30 μM of IT. Data represents mean ± std.dev, n=15 intensity profiles from six different cells.

A

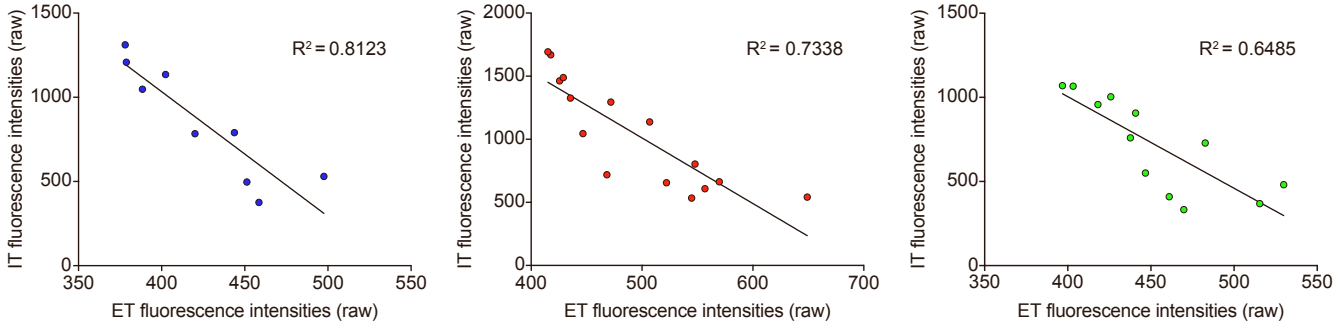

B

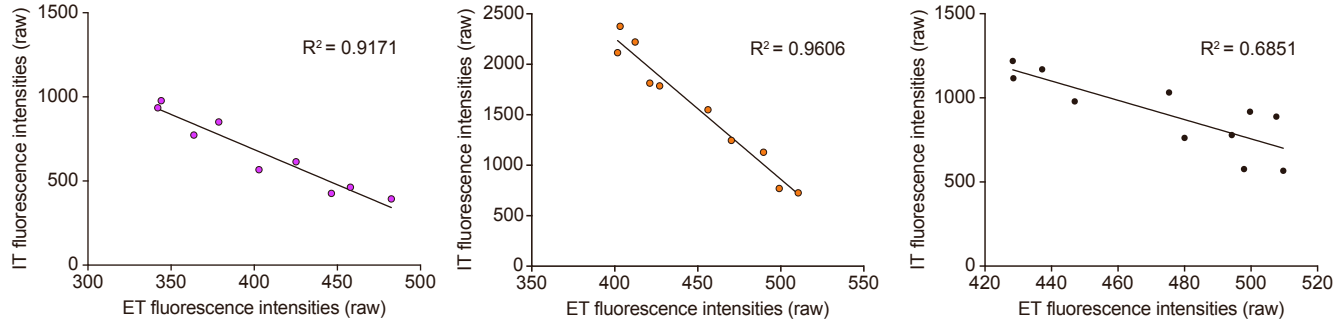

C

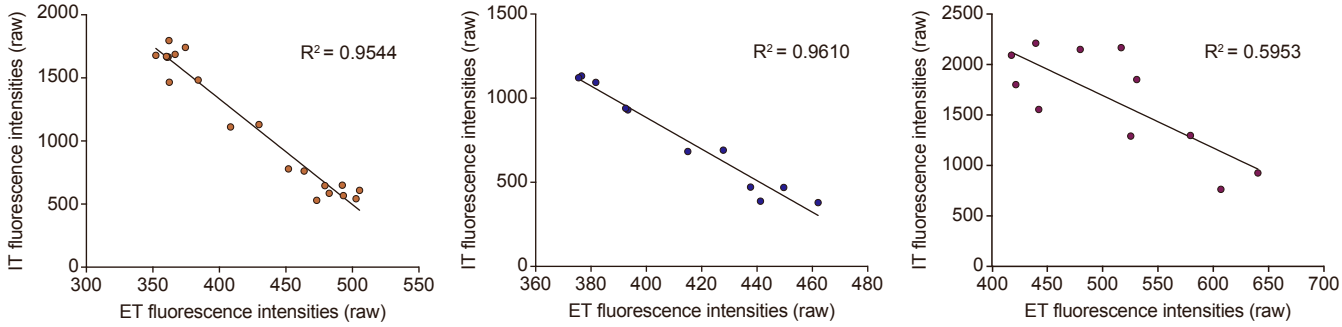

D

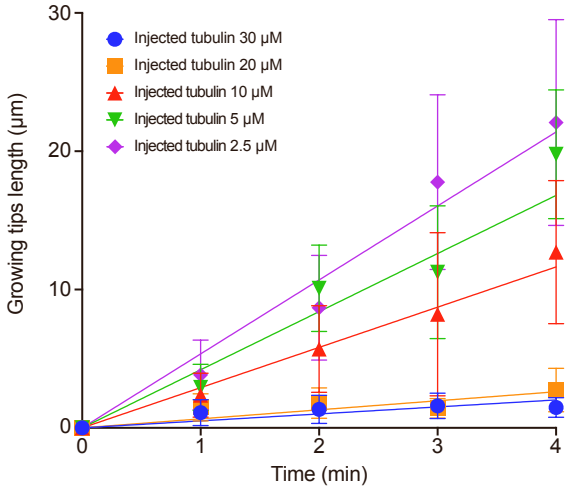

E

Concentrations of IT	Rate of elongation	
2.5 µM	5.348 µm.min^{-1}	89.13 nm.sec^{-1}
5 µM	4.202 µm.min^{-1}	70.03 nm.sec^{-1}
10 µM	2.909 µm.min^{-1}	48.48 nm.sec^{-1}
20 µM	0.6527 µm.min^{-1}	10.88 nm.sec^{-1}
30 µM	0.505 µm.min^{-1}	8.42 nm.sec^{-1}

Figure S3: Anti-correlation between injected tubulin intensity and endogenous tubulin intensity in patch of injected tubulin, and dependance of labelled tubulin concentration in microtubules elongation rate, Related to Figure 2 and Figure 4.

(**A**) Correlations between injected tubulin intensities and expressed tubulin intensities measured in three different linescans in cells microinjected with 10 µM of IT. R squared were measured using linear regression. (**B**) Correlations between injected tubulin intensities and expressed tubulin intensities measured in three different linescans in cells microinjected with 20 µM of tubulin. R squared were measured using linear regression. (**C**) Correlations between injected tubulin intensities and expressed tubulin intensities measured in three different linescans in cells microinjected with 30 µM of tubulin. R squared were measured using linear regression. (**D**) Measurement of growing tips length over time in cells microinjected with 2.5, 5, 10, 20, 30 µM of IT. Data represents mean ± std.dev., n=105-341 growing tips measured in 7-17 cells for each condition. (**E**) Table with the slopes of corresponding linear regressions measured for each IT concentration.

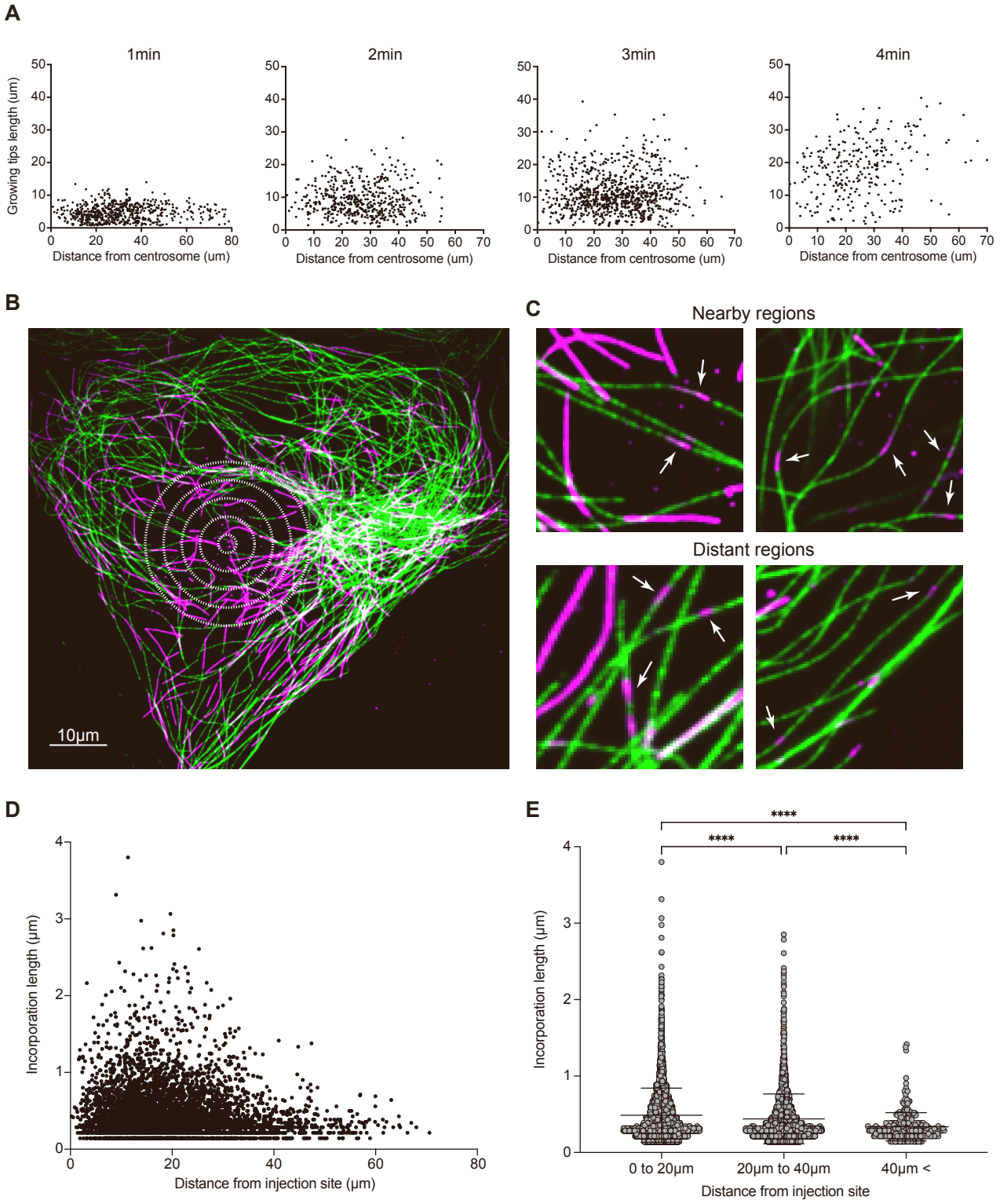
A
1min
2min
3min
4min
Growing tips length (um)
Distance from centrosome (um)
B
10μm
C
Nearby regions
Distant regions
D
Incorporation length (μm)
Distance from injection site (μm)
E
****
****
****
Incorporation length (μm)
0 to 20μm
20μm to 40μm
40μm <
Distance from injection site

Figure S4: Microtubule elongation rate through PTK2 cytoplasm and distribution of incorporation length depending on the distance to the injection site, Related to Figure 4 and Figure 5.

(**A**) Length of newly polymerized growing tips after the injection of 5 uM of IT, relative to the position of the centrosome. Data represents 645, 495, 874 and 271 growing tips measured for 1, 2, 3 and 4 minutes, respectively. (**B**) Representative image of PtK2 GFP-tubulin cell microinjected with 10 µM of tubulin. White concentric circles are representing the injection site. Scale bar, 10 µm. (**C**) Enlarged regions of nearby and distant regions from two different cells. White arrows are showing the presence of magenta IT incorporations in the pre-existing microtubule network. (**D**) Dot plot of incorporation lengths as a function of the distance from the injection site. (**E**) Incorporation lengths measured as a function of the distance from the injection site grouped by 20 µm size ranges. In **D** and **E**, n=5703 incorporations measured from 111 cells used in the whole study.

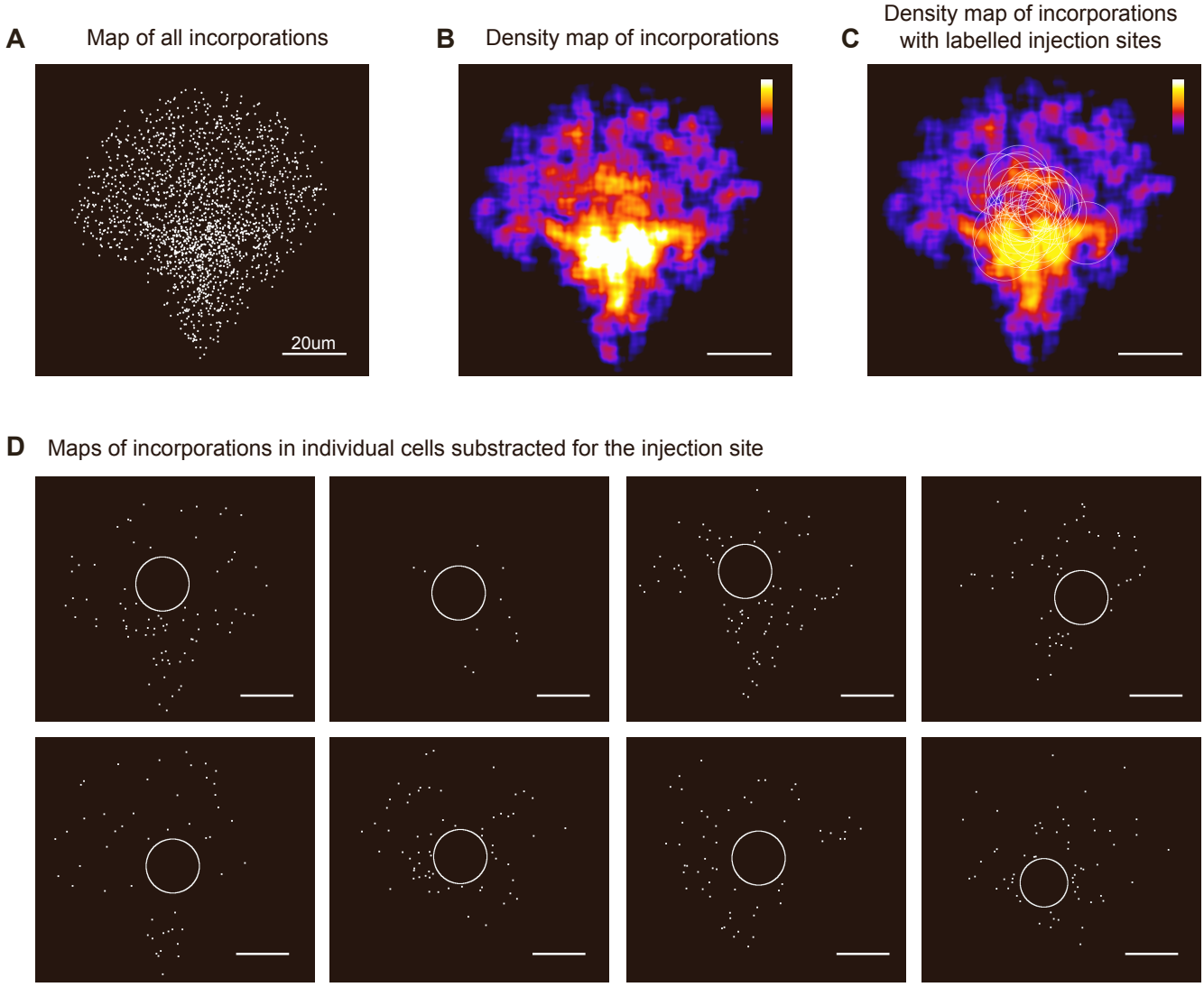

Figure S5: Workflow for the removal of incorporations close to the injection site in crossbow patterned PtK2 cells, Related to Figure 5.

(**A**) Overlay of the positions of incorporations measured in 34 cells from six independent experiments. (**B**) Density map of incorporations measured in **A**. The distribution of positions was spatially averaged using a 40-pixel-wide sliding square and color coded with the "fire" look-up table. (**C**) Density map of incorporations measured in **B** with labelled injection sites. (**D**) Maps of incorporations in individual cells after subtraction of incorporations in the injection site. Scale bars, 20 µm.